RESEARCH ARTICLE
SOLID EARTH: COMPUTATIONAL GEOPHYSICS

Earth and Planetary Physics
6: 399–423, 2022
doi: 10.26464/epp2022035

The anisotropy of hexagonal close-packed iron under inner core conditions: the effect of light elements

Wei Zhang[1], Mei Tang[2], and ZhenWei Niu[1,3]*

[1]Laboratory for Extreme Conditions Matter Properties, Southwest University of Science and Technology, Mianyang Sichuan 621010, China;

[2]Fundamental Science on Nuclear Wastes and Environmental Safety Laboratory, Southwest University of Science and Technology, Mianyang Sichuan 621010, China;

[3]School of National Defense Science & Technology, Southwest University of Science and Technology, Mianyang Sichuan 621010, China

Key Points:

- The structure-anisotropy relationship of binary hcp-Fe alloys are investigated at Earth's inner core condition.
- The Earth's inner core may be an oxygen-depleted environment.
- The anisotropy of binary hcp-Fe alloys depends on the combined effects of temperature and the type of light elements.

Citation: Zhang, W., Tang, M., and Niu, Z. W. (2022). The anisotropy of hexagonal close-packed iron under inner core conditions: the effect of light elements. *Earth Planet. Phys.*, *6*(4), 399–423. http://doi.org/10.26464/epp2022035

Abstract: In recent decades, global seismic observations have identified increasingly complex anisotropy of the Earth's inner core. Numerous seismic studies have confirmed hemispherical variations in the inner core's anisotropy. Here, based on *ab initio* molecular dynamics calculations, we report how the anisotropy of hexagonal close-packed (hcp)-iron, under inner core conditions, could be altered when alloyed with light elements. We find that light elements in binary allows with iron — hcp-Fe-X (X = C, O, Si, and S) — could have significant effects on density, sound velocities, and anisotropy, compared with the behavior of pure hcp-iron; the anisotropy of these binary alloys depends on combined effects of temperature and the particular alloying light element. Furthermore, the change in anisotropy strength with increasing temperature can be charted for each alloy. Alloying pure iron with some light elements such as C or O actually does not increase but decreases core anisotropy at high temperatures. But the light element S can significantly enhance the elastic anisotropy strength of hcp-Fe.

Keywords: iron; elastic constants; anisotropy; inner core

1. Introduction

Seismic observations have increasingly confirmed that longitudinal waves across the Earth's solid inner core travel faster along the polar axis than in the equatorial plane (Morelli et al., 1986; Woodhouse et al., 1986). The earliest explanation offered to explain this anisotropy, thirty years ago, was that crystalline iron, the main component of the Earth's inner core, is intrinsically anisotropic (Jeanloz and Wenk, 1988; Wenk et al., 2000; Buffett and Wenk, 2001). Nevertheless, recent research has suggested that the anisotropy of Earth's inner core may be more complex and interesting than we have realized (e.g. Niu FL and Wen LX, 2002; Lythgoe et al., 2014; Wang T et al., 2015; Romanowicz et al., 2016). This anisotropy is not uniform in the whole inner core, and it becomes stronger with the increase of depth. Furthermore, significant hemispherical differences have also been observed: the eastern hemisphere has a relatively weak anisotropy, of about 0.5–1.5%, whereas the western hemisphere has a strong anisotropy — about 3.5–8.8% with the increase of depth (Lythgoe et al., 2014). These observations suggest that the inner core may be heterogeneous in composition, which would bring a clear challenge to the related mineralogy: What form of iron would produce the observed 3.5–8.8% seismic anisotropy in the western hemisphere of the inner core, given known conditions in the core? (Lincot et al., 2015; Romanowicz et al., 2016; Romanowicz and Wenk, 2017).

There has been general agreement that the most possible phase of core iron is the hcp-structure, which has a strong anisotropy. Recently, experimental work (e.g., Tateno et al., 2010, 2012) strengthened confidence that the hcp-crystalline structure is indeed most likely to be the structure of pure iron and relevant alloys at inner core conditions. However, different studies have yielded greatly different degrees of anisotropy for hexagonal close-packed iron. The corresponding longitudinal wave anisotropies do not exceed 8% (e.g. for Mattesini et al., 2010, 5.7% at 364 GPa), which lies below the maximum observed seismic anisotropy of 8.8% in the western hemisphere of the inner core reported by Lythgoe et al. (2014). Besides, it must be observed that an anisotropy of only 8.8% is not adequate, because a huge single crystal of iron could not possibly exist in the inner core. Clearly, compositions and behaviors of greater complexity should

Correspondence to: Z. W. Niu, z.w.niu@foxmail.com
Received 21 FEB 2022; Accepted 15 APR 2022.
Accepted article online 02 JUN 2022.

be considered, such as possible new phases beyond the hcp-phase and possible alloying of the iron with light elements in the inner core. Hence, to throw greater light upon the phenomenon of seismic anisotropy and upon inner core structures more generally, detailed knowledge of the elasticity of iron and iron alloys under complicated conditions would seem to be a promising approach.

Although many phases, such as face-centered cubic (fcc) or body-centered cubic (bcc) (Belonoshko et al., 2003, 2017), seem possible at inner core conditions, a large number of experiments have concluded that the hcp-phase remains the most likely structure (e.g., Tateno et al., 2010, 2012; Merkel et al., 2013). Hence, in the present study, we focus on the effects of light elements on the hcp-phase rather than other phases; other phases will be considered in the future. From a standpoint of materials science, light elements can significantly affect the key properties of hcp-iron, such as density and anisotropy. The Earth's inner core is thought to contain ~10 wt.% light elements, the most probable of which include C, Si, O, S, and H (e.g., Vočadlo, 2007; Belonoshko et al., 2007; Martorell et al., 2013b, 2016; Li YG et al., 2016, 2018; Hirose et al., 2017). The effect of these light elements on the core's anisotropy can be explored by assuming that core iron is alloyed with these different light elements. Many studies have been performed to explore such alloy structures and their properties (e.g. Lin JF et al., 2003; Fischer et al., 2014; Li YG et al., 2018). Fischer et al. (2013, 2014) determined the phase relations and equations of state of part Fe-Si alloys at high pressures and temperatures, and found that iron and silicon atoms have similar volumes at high pressures. By combining a solid solution model with direct simulations on the ternary hcp-Fe alloys, Li YG et al. (2018) reported a number of compositions that appear able to match the observed properties of the inner core. However, despite that result, a detailed investigation of the anisotropy of hcp-iron alloyed with light elements has been needed, to determine whether hcp-iron and iron alloys can adequately explain all observed details of the seismic anisotropy.

In this study, to investigate in detail the impact of light elements on the anisotropy of core iron, we focus on the thermoelasticity of hcp-iron alloyed with C, Si, O, and S under inner core conditions. Although Ni is also a possible core element, it can be safely ignored due to the negligible effect of Ni content on the anisotropy of iron at inner core pressures and temperatures (Martorell et al., 2013a).

2. Methods

2.1 *Ab Initio* Calculations

The calculations in this work were performed using density functional theory (DFT) as implemented in the Vienna *ab initio* Simulation Package (VASP) (Kresse and Furthmüller, 1996). The projector augmented wave (PAW) approach was used for describing the electron-ion interaction, with energy cutoffs of 500 eV (Blöchl, 1994; Kresse and Joubert, 1999). We employed a hard version of the PAW potential that is specially designed for high pressure applications. The effects of exchange-correlation interaction were treated within the generalized gradient approximation (GGA) in the scheme of the Perdew–Burke–Ernzerhof (PBE) formula (Perdew et al., 1996). The self-consistent convergence of the total energy was 1.0×10^{-6} eV/atom, and the maximum ionic Hellmann-Feynman force was set to 0.01 eV/Å. For all necessary convergence tests, total energy change was held below 1.0×10^{-4} eV/atom by increasing cut-off energy and k meshes in the Brillouin-zone.

The *ab initio* molecular dynamics (AIMD) calculations were performed within the NVT ensemble with Nosé–Hoover thermostat (Nosé, 1984) at different volumes and three temperatures, 2000 K, 4000 K, and 6000 K. The time step for the ion motion was set to 1 fs. Electron temperature refers to the kinetic energy generated by the movement of electrons and the temperature changes at the same time. Here, the Fermi–Dirac function (Mermin, 1965) was used to describe the electron contribution to free energy at finite temperature. The supercells with both 64 and 128 atoms were tested; mainly, we used the supercell of 64 atoms due to the fact that the calculations with 128 atoms supercell were too expensive. In these AIMD calculations, Gamma k-point, 4 irreducible k-points, and 8 irreducible k-points were tested; most of our results were based on 4 irreducible k-points, arrrived at by balancing reliability of the obtained results against computational cost. We ran the AIMD simulations of several structures for up to 10 ps and found that results at higher ps agree with the simulation run between 6 and 8 ps. Thus, all AIMD simulations were run at 8 ps to give reasonably accurate results using the least expensive levels of theory. A time step of 1 fs was used for the integration; the AIMD data were recorded every 2 fs. To reach reasonable convergence, a minimum of eight electronic steps was also forced to run for each ionic step. The time-averaged lattice parameters were determined from the recorded data, based on the last 2 ps of the simulation. The final temperatures and stresses were averaged excluding the first 2 ps. The statistical errors were evaluated by the blocking method for correlated data (Flyvbjerg and Petersen, 1989). The standard deviation is defined as:

$$\sigma \approx \sqrt{\frac{c_0'}{n'-1}\left(1+\frac{1}{\sqrt{2\left(n'-1\right)}}\right)}, \tag{1}$$

where $n' = n/2$, $c_0' = \frac{1}{n'}\sum_{k=1}^{n'}(x_k - \bar{x})^2$, and $x_i' = \frac{1}{2}(x_{2i-1} + x_{2i})$. The evaluation of the final statistics in temperature shows that the statistical errors are less than 0.5% in all cases.

2.2 Elastic Properties Calculations

The isotropic elastic constants were obtained via the strain–stress relationship (Page and Saxe, 2002). The elastic tensor is obtained by performing six finite distortions of the lattice and deriving the elastic constants from the strain–stress relationship $\sigma_{ij} = c_{ijkl}\varepsilon_{kl}$. The six distortion are $\varepsilon(\delta) = (\delta, 0, 0, 0, 0, 0)$, $(0, \delta, 0, 0, 0, 0)$, $(0, 0, \delta, 0, 0, 0)$, $(0, 0, 0, \delta, 0, 0)$, $(0, 0, 0, 0, \delta, 0)$, and $(0, 0, 0, 0, 0, \delta)$, where δ is the magnitude of the strain (±0.6%, ±0.4%, and ±0.2%). We choose these strains because the crystal is likely to be beyond linear elasticity when the strain is in excess of 1%; strains of 0.1% and below will generate a set of structures that are very similar to one another. Then, for a given strain pattern and strain amplitude, the

stresses on the simulation box were obtained from NVT simulations run over ~8 ps. Each of them represents a geometry optimization run at a fixed cell. Elastic moduli, including the corresponding uncertainty, are obtained from the results of linear fitting for each strain pattern. To obtain the elastic constants at certain pressures, linear fitting is used here to fit the elastic constants and pressures computed from our simulations. To demonstrate the validity of elastic constants, we calculate the Degree-of-Freedom adjusted coefficient of determination (Adj. R-Square) and analyze the linear fitting variance. Therefore, the final error estimates of the elastic constants reflect three uncertainties: statistical errors of the stresses, of the linear fitting of stresses and strains, and of the linear fitting of the elastic constants and pressure.

An important problem is the break of symmetry with the addition of light elements. The hexagonal lattice symmetry will be breached and will follow triclinic symmetry. The triclinic tensor can be projected to the hexagonal tensor using the following relationship: $\boldsymbol{C}_{\text{hexagonal}} = \boldsymbol{P} \cdot \boldsymbol{C}_{\text{triclinic}}$, where $\boldsymbol{P}$ is the projector matrix defined by Moakher and Norris (2006). Our calculations of elastic constants follow the triclinic symmetry at finite temperature, but the simulation box remains hexagonal in structure, which ensures the reliability of the projection. On the other hand, Li YG et al. (2018) compared elastic constants obtained from the projector matrix and directly calculated following the hexagonal symmetry, and found the difference to be insignificant, with the exception of C_{44}, for which the difference in aggregated properties was small. These results confirm the reliability of the projection approach.

There are two approximation methods to calculate the polycrystalline modulus, namely Voigt method (Voigt, 1928) and Reuss method (Reuss and Angew, 1929). For the hexagonal structure, the bulk and shear moduli using Voigt method (B_{V}, G_{V}) and Reuss method (B_{R}, G_{R}) are given by

$$B_{\text{V}} = \frac{1}{9}\left[2\left(C_{11}+C_{12}\right)+C_{33}+4C_{13}\right], \tag{2}$$

$$B_{\text{R}} = \frac{\left(C_{11}+C_{12}\right)C_{33}-2C_{13}^2}{C_{11}+C_{12}+2C_{33}-4C_{13}}, \tag{3}$$

$$G_{\text{V}} = \frac{1}{30}\left(C_{11}+C_{12}+2C_{33}-4C_{13}+12C_{44}+12C_{66}\right), \tag{4}$$

$$G_{\text{R}} = \frac{5}{2}\frac{\left(\left(C_{11}+C_{12}\right)C_{33}-2C_{13}^2\right)^2 C_{44}C_{66}}{3B_{\text{V}}C_{44}C_{66}+\left(\left(C_{11}+C_{12}\right)C_{33}-2C_{13}^2\right)^2\left(C_{44}+C_{66}\right)}. \tag{5}$$

The Voigt–Reuss–Hill (VRH) average is used to estimate elastic modulus of polycrystals (Hill, 1952). The VRH averages for shear and bulk moduli are

$$G = \frac{1}{2}\left(G_{\text{R}}+G_{\text{V}}\right), \tag{6}$$

$$B = \frac{1}{2}\left(B_{\text{R}}+B_{\text{V}}\right). \tag{7}$$

The isotropic wave propagation velocities (v_{p} and v_{s}) can be evaluated via the above elastic moduli, together with the density ρ from Navier's equation (Panda and Chandran, 2006):

$$v_{\text{p}} = \sqrt{\left(B+\frac{4}{3}G\right)/\rho}, \quad v_{\text{s}} = \sqrt{G/\rho}. \tag{8}$$

The relative P-wave velocities are related to the elastic constants by the Christoffel equation:

$$k^2\left(l_{iK}C_{KL}l_{Lj}\right)v_j = k^2\Gamma_{ij}v_j = \rho\omega^2 v_i. \tag{9}$$

where $\Gamma_{ij} = l_{iK}C_{KL}l_{Lj}$. The matrix element of Γ_{ij} is a function of elastic constants and directions of plane waves. For hexagonal symmetry crystals, the corresponding Christoffel equation can be represented as:

$$k^2\begin{bmatrix} C_{11}l_x^2+C_{66}l_y^2+C_{44}l_z^2 & \left(C_{12}+C_{66}\right)l_xl_y & \left(C_{13}+C_{44}\right)l_xl_z \\ \left(C_{12}+C_{66}\right)l_xl_y & C_{66}l_x^2+C_{11}l_y^2+C_{44}l_z^2 & \left(C_{13}+C_{44}\right)l_yl_z \\ \left(C_{13}+C_{44}\right)l_xl_z & \left(C_{13}+C_{44}\right)l_yl_z & C_{44}l_x^2+C_{44}l_y^2+C_{33}l_z^2 \end{bmatrix}\times\begin{bmatrix} v_x \\ v_y \\ v_z \end{bmatrix} = \rho\omega^2\begin{bmatrix} v_x \\ v_y \\ v_z \end{bmatrix}. \tag{10}$$

The phase velocities in different mediums can be deduced from the relationship $v_{\text{p}} = \omega/k$. In the case of cylindrical symmetry and P-wave propagation, the Christoffel equation can be reduced to:

$$\begin{aligned}\rho v_{\text{p}}^2(\xi) = {} & C_{11}+\left(4C_{44}+2C_{13}-2C_{11}\right)\cos^2(\xi) \\ & +\left(C_{33}+C_{11}-4C_{44}-2C_{13}\right)\cos^4(\xi),\end{aligned} \tag{11}$$

where $v_{\text{p}}(\xi)$ is the longitudinal acoustic velocity along the angle ξ. If the seismic anisotropy of the inner core is assumed to be dominated by cylindrical anisotropy, a perturbation to a spherically symmetric model can be expressed as (Creager, 1992)

$$\frac{\delta t}{t} = -\frac{\delta v}{v} = a+b\cos^2\zeta+c\cos^4\zeta, \tag{12}$$

where v and δv present the P-wave velocity and the velocity perturbation in the reference model, t and δt are the time the ray spends and the measured travel time residual in the inner core, and ζ is the angle between the inner core ray path and the rotation axis. Combining Equation (11), if all crystals are aligned in one direction, the travel time residual can be approximated by

$$\frac{\delta t}{t} = -\frac{\delta v_{\text{p}}}{v_{\text{p0}}}, \tag{13}$$

where v_{p0} is the average velocity and δv_{p} is the difference between v_{p} and v_{p0}. It should be noted that use of the different averaging methods mentioned above could cause a positive or negative impact on v_{p0}.

2.3 The Process of Structure Optimization

First, pure hcp-iron was optimized in the pressure range of the inner core and at zero temperature; the obtained optimal structures were then extended to 4 × 4 × 2 supercells. Next, the light elements were introduced by replacing iron atoms in different positions of the supercells. To determine the lowest energy structure, Gibbs free energies were calculated for each supercell with the replacing atom at a different position. The obtained lowest energy structure for each different replacement was used in the

following calculations. Equilibrium optimization procedures were then conducted: first, for a fixed volume V, we took a series of different axial ratios c/a to calculate the total energies E, and thus determine the lowest energy $E_{\min}$ for the given volume V and its corresponding lattice parameters (c and a). In these energy calculations, the $9\times9\times9$ Γ-centered k meshes were used. This procedure was repeated over a wide range of V. Finally, by fitting $E_{\min}$–V data to the third-order Birch–Murnaghan equation of state (EOS)

$$E(V)=-\frac{9}{16}\left[\left(4-B_0'\right)\frac{V_0^3}{V^2}-\left(14-3B_0'\right)\frac{V_0^{7/3}}{V^{4/3}}+\left(16-3B_0'\right)\frac{V_0^{5/3}}{V^{2/3}}\right]+E_0, \tag{14}$$

the equilibrium cell volume V_0, the bulk modulus B_0, and its pressure derivative B_0' were harvested. The equilibrium lattice parameters c, a, and c/a were then available. The equilibrium pressures emerge from the relationship: $P(V)=-\partial E/\partial V$. Considering that the anisotropy of hcp-structured materials may be related to the c/a axial ratio, the initial structure parameters were carefully optimized. The c/a ratios of the lattice parameters for $Fe_{60}C_4$, $Fe_{60}O_4$, $Fe_{60}Si_4$, and $Fe_{60}S_4$, respectively, were 1.58, 1.57, 1.59, and 1.60 in the pressure range of the inner core. For $Fe_{56}X_8$ (X= C, O, Si, and S), the c/a ratios were 1.59, 1.55, 1.60, and 1.60, respectively. A slight increase of the c/a ratios was found with increasing pressure in the core pressure range.

Considering the change of c/a with temperature, the following procedures were performed to determine the equilibrium axial ratio c/a at finite temperatures. For a simulation box with fixed volume V, a series of different axial ratios c/a were adopted to run finite temperature *ab initio* molecular dynamics. The equilibrium axial ratio c/a corresponding to the lowest statistical average energy $\bar{E}_{\min}$ could then be obtained by numerical fitting the data of statistical average energy $\bar{E}$ and axial ratio c/a at the given volume V. In the following, finite temperature *ab initio* molecular dynamics was performed in the simulation box with the equilibrium axial ratio c/a for the given volume V. This procedure was repeated for the full range of volumes V considered here. A unit cell to calculate the corresponding isothermal elastic constants was then constructed from the average lattice parameters from these NVT simulations based on the equilibrium axial ratios c/a. To reduce the impact of statistical error, this unit cell was relaxed around the equilibrium axial ratio c/a before the calculation of elastic constants; that is, keeping the ions and the cell volume fixed, the cell shape was allowed to change. This relaxed unit cell was then used as the initial configuration (the one subjected to strains) in the process of calculating the elastic constants. In addition, the initial configuration was initially under quasi-hydrostatic pressure that was very close to known hydrostatic pressure (the deviations were kept to less than 0.2%). The quasi-hydrostatic pressure is the average force from *XX*, *YY*, and *ZZ* directions in the NVT simulations with the equilibrium axial ratio c/a.

3. Results and Discussion

3.1 Structure, Density, and Sound Velocity of Binary hcp-Fe Alloys

As a key structure parameter, the unit cell axial ratio (c/a) has a direct effect on the elastic anisotropy of hcp-Fe and its alloys. In our calculations, the c/a axial ratios at high pressures and temperatures are fully considered with the minimum energy principle; see Figure 1. We find that the c/a ratio changes with temperature: for hcp-Fe, this ratio increases from slightly less than 1.59 at low temperature to 1.61 at 6000 K. However, compared with the impact of temperature, the temperature variation of the axial ratio can be ignored as pressures approach the inner core. The yielded axial ratio of pure hcp-Fe (1.605 at 333 GPa and 6000 K) is in close agreement with the experiment of Tateno et al. (2010) (1.602 at 332 GPa and 4820 K). This ratio also agrees with the calculation of Belonoshko et al. (2004), Steinle-Neumann et al. (1999), and Niu ZW et al. (2015), although it is significantly lower than the calculation of Vočadlo et al. (2009). The resulting c/a is ~1.59 at inner core pressure and 0 K, which is in good agreement with the linear response result (~1.591) reported by Sha XW and Cohen (2006). The ratio c/a has a direct effect on the elastic anisotropy of hcp-Fe, and hcp-Fe tends to be isotropic at high temperature if c/a is close to ideal axial ratio of 1.633. According to linear response result, Sha XW and Cohen (2010a, b) claimed that both the compressional and shear waves of hcp-Fe become elastically isotropic under the Earth's inner core conditions, where the volume of hcp-Fe is ~46 bohr^3/atom. The corresponding c/a is likely to be higher than 1.609 and close to 1.633, because Sha XW and Cohen (2006) calculated c/a to be ~1.609 using linear response method at the volume of 50 bohr^3/atom and 6000 K. In our AIMD simulation, c/a is ~1.607 under the Earth's inner core conditions (360 GPa, 6000 K, and ~46 bohr^3/atom), at which hcp-Fe is still substantially anisotropic. The axial ratios of the binary hcp-Fe alloys increase with temperature with a variation trend similar to that of hcp-Fe, and are far below the ideal axial ratio of hcp-Fe (1.633). There exists measurable distinctions among the axial ratios of hcp-Fe alloyed with different light elements. The axial ratios of $Fe_{60}X_4$ (X = C, O) are ~0.01 below those of pure iron at 2000 K and ~0.005 below at 4000 K, but both are close to each other at 6000 K; the axial ratios of $Fe_{60}X_4$ (X = S, Si), however, become larger than those of pure iron at high temperatures. In comparison with $Fe_{60}X_4$ (X = C, O, S, Si), for $Fe_{56}X_8$ (X = C, O, S, Si), the light elements have more substantial impact on the axial ratio c/a of hcp-Fe at finite temperature. Different light elements show entirely different influence on the axial ratio of hcp-Fe. C and O substitutions reduce the axial ratio significantly. For instance, the axial ratio of $Fe_{56}O_8$ is ~1.58 at ~360 GPa and 6000 K, which is obviously lower than that of hcp-Fe (~1.61) at the same conditions. But alloying iron with S results in a huge increase of the axial ratio of hcp-Fe. The axial ratio of $Fe_{56}S_8$ is ~1.62 at 4000 K under inner core pressures, and then reaches and even exceeds 1.625 at 6000 K, much larger than that of hcp-Fe (~1.61) and close to the ideal axial ratio of hcp-Fe (1.633) where hcp-Fe tends to be isotropic. This also explains why the anisotropy strength of relative P-wave velocity exhibits a remarkable decrease at 6000 K, compared with 4000 K, in our calculations with pressures below 360 GPa. Alloying iron with light elements therefore has an impressive influence on the c/a axial ratio of pure iron, which is in agreement with available experimental results from Morrison et al. (2018), Lin JF et al. (2003), and Tateno et al. (2012).

Several general conclusions can be drawn about the c/a axial ratios: axial ratios increase negligibly with increasing pressure at a

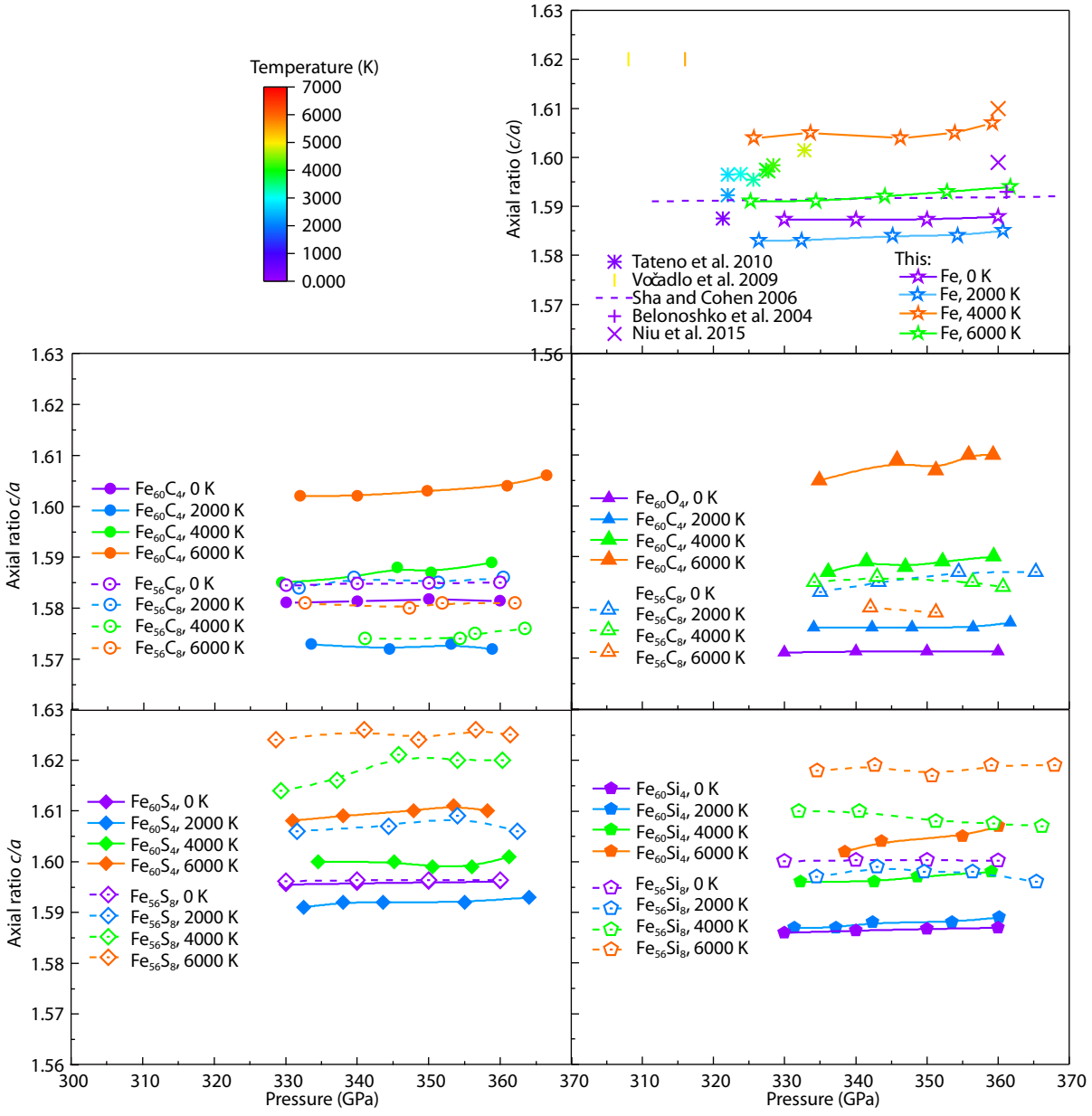

Figure 1. Calculated axial ratios *c/a* for hcp-Fe and binary hcp-Fe alloys.

given temperature; when pressure is fixed, changes in *c/a* are not always correlated positively with finite temperature change; at inner core conditions, the *c/a* axial ratio is influenced significantly both by temperature and by type of light element alloyed with iron.

As the most important physical quantity for core modeling, density is one of the few that can be directly compared with seismic observations. Iron is proposed as the dominant element of the inner core, but it is too dense with respect to seismic models. In order to match seismic models (e.g. Beghein and Trampert, 2003; Wang T et al., 2015), some light elements with different content need to be introduced. The pressure of the inner core varies from ~330 GPa at the boundary of inner and outer core to ~364 GPa at the inner core's center; our simulations focus primarily on the pressure range of the inner core at different temperatures. Figure 2 illustrates the changes of the densities of different binary alloys with temperature and pressure, and the densities as a function of temperature at 360 Ga are compared with previous *ab initio* molecular dynamics simulations in Figure 3. The density-pressure relationship of pure hcp-Fe at 0 K is far above the Preliminary Reference Earth Model (PREM) data (Dziewonski and Anderson, 1981), but it agrees well with the extrapolation from experimental data at high pressure and ambient temperature (Sakai et al., 2014). There occurs a drop of 4.5% at 330 GPa and a drop of 3.7% at 360 GPa when temperature increases to 6000 K. The density at 360 GPa and 6000 K is predicted to be 13.67 g/cm^2, which is significantly higher than the PREM data but close to previous results obtained with *ab initio* methods (Martorell et al., 2013a, b; Niu ZW et al., 2015). We note that only Li YG et al. (2018) has reported a slightly lower density at high temperatures, which may be due to the difference between their structure models and ours. For binary alloys $Fe_{60}X_4$ (X = C, O, Si, and S), the introduction

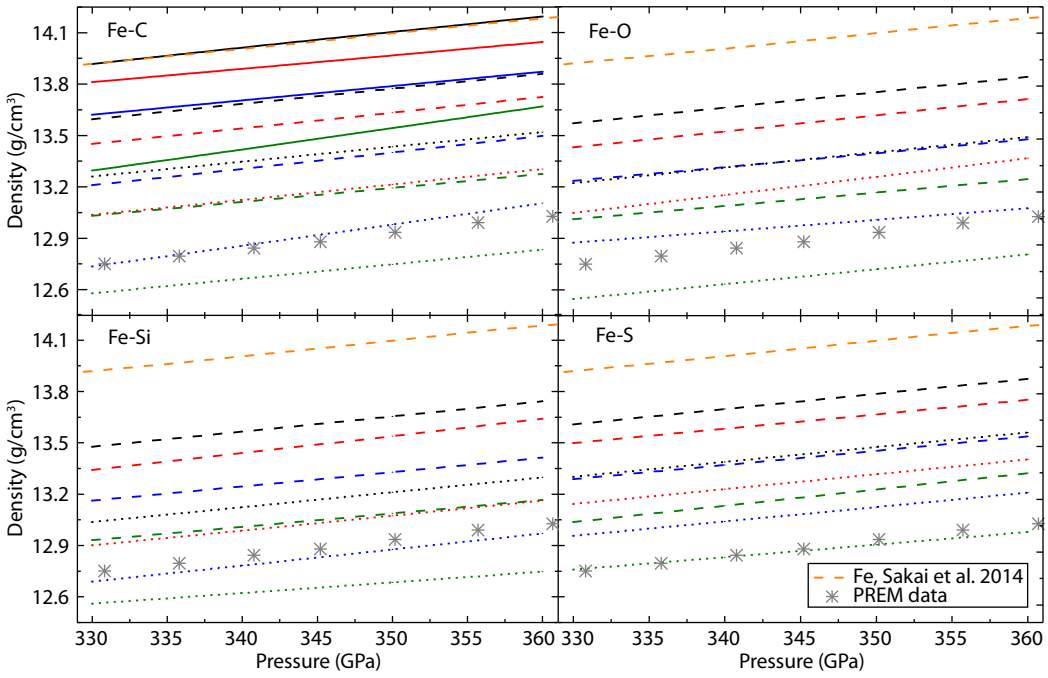

Figure 2. Calculated densities as functions of pressures at different temperatures for pure iron, $Fe_{60}X_4$, and $Fe_{56}X_8$ (X = C, O, Si, and S). The solid, dash, and short dash lines represent the densities of pure iron, $Fe_{60}X_4$, and $Fe_{56}X_8$ (X = C, O, Si, and S), respectively. The black, red, blue, and green hues signify 0 K, 2000 K, 4000 K, 6000 K, respectively.

of light elements causes a significant decrease of density compared to pure iron. The densities remain higher than PREM data for temperatures not exceeding 6000 K, although a significant drop is observed. It is worth noting that $Fe_{60}C_4$ is already unstable and melts at 5500 K — see Li YG et al. (2018), while we find that $Fe_{60}C_4$ and even $Fe_{56}C_8$ are still stable at 6000 K. First, the difference is probably attributable to different judgments of melting criteria. In our calculations, melting is assumed to occur when the second peak disappears in the radial distribution function (Figure S1a) and the root-mean-square displacements (Figure S1b) continuously increase with time (Martorell et al., 2013b; Ganz et al., 2017). Second, different theory methods can also lead to the differences. Compared with the *ab initio* molecular dynamics (AIMD) methods within the NPT ensemble used in Li YG et al. (2018), our calculations

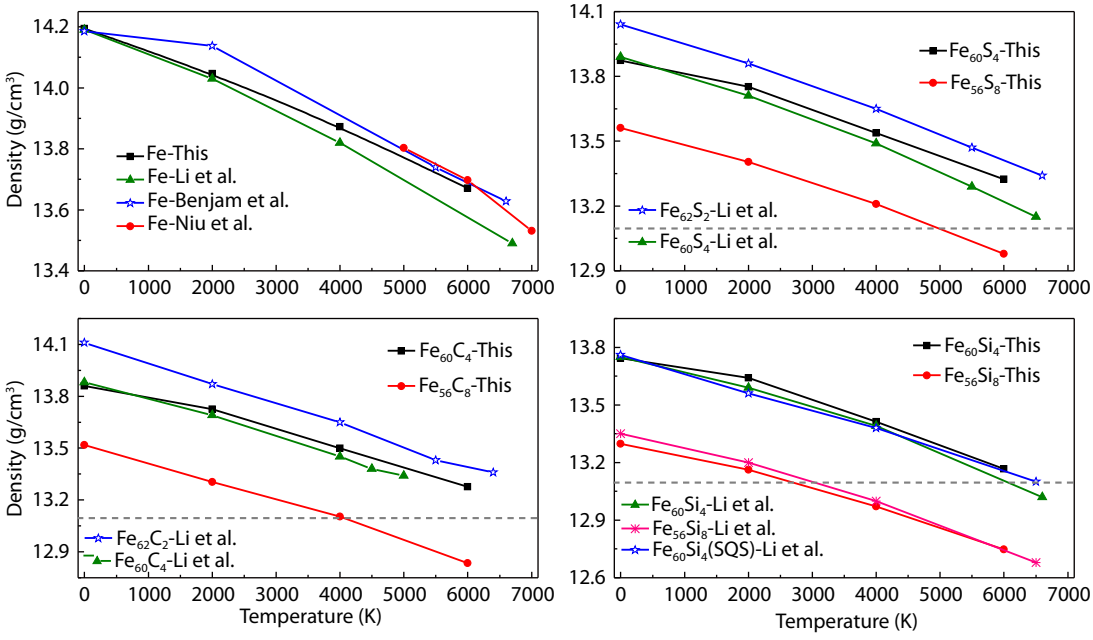

Figure 3. Calculated density of pure iron, $Fe_{60}X_4$, and $Fe_{56}X_8$ (X = C, Si, and S) as a function of temperature at 360 GPa. The dashed lines stand for the PREM data.

utilize the AIMD within the NVT ensemble. In addition, it should be noted that Si leads to the most significant density decrease of hcp-Fe compared with other light element hcp-Fe alloys in the same stoichiometric ratio, which agrees with the previous report of Li YG et al. (2018). Moreover, the obtained relationships of density and temperature at 360 GPa are consistent with those of Li YG et al. (2018).

For another kind of binary alloy $Fe_{56}X_8$ (X = C, O, Si, and S), different elements have significantly different impacts on density. At 6000 K, the densities of $Fe_{56}X_8$ (X = C, O, and Si) at all inner core pressures lie far below the PREM data, while the density of $Fe_{56}C_8$ at 330 GPa and the density of $Fe_{56}Si_8$ at all applied pressures and are slightly lower than the PREM data at 4000 K. With regard to $Fe_{56}S_8$, only at 360 GPa and 6000 K the density is slightly lower than the PREM data. Though the disordered structures are more relevant to the Earth's core, the effect on the density can be reasonably ignored with very few exceptions (Li YG et al., 2018). By comparing these AIMD results, which considered only pure hcp-Fe-Si binary alloy, the content of Si in the inner core falls within 3.23–6.67 wt.%; this result coincides with the estimation of 4–8 wt.% given by ideal mixing models (Lin JF et al., 2003; Asanuma et al., 2011; Fischer et al., 2014). For S, a potential element in the inner core that has commonly been found in meteorites (Alfè et al., 2000), the amount is at least 7.55 wt.% for pure hcp-Fe-S binary alloy. This agrees well with the estimation of 6.4–8.4 wt.% based on the equation of state of Fe_2S (Bazhanova et al., 2017). For C and O, their content may not exceed 2.97 wt.% and 3.92 wt.% in corresponding pure binary alloys. It is important to note that the slopes of density with pressure for these binary alloys are close to those of the PREM data. The resulting slopes of the curves between density and pressure at fixed temperature approach the PREM data; however, single binary hcp-Fe alloy may be an insufficient candidate in the inner core, because the temperature of the inner core is not a constant but rises with the depth.

Density is less precisely determined by seismic observations than is sound velocity. Thus, tighter constraints on compositional models of the inner core can be obtained by comprehensive comparisons of density, sound velocity, and related anisotropy of candidate alloys with seismic models. Figure 4 depicts the variation of the compressional sound velocity (v_p) for different binary alloys from 0 K to 6000 K at core pressures. For binary alloys $Fe_{60}X_4$ (X = C, O, Si, and S), the compressional sound velocities decrease by 1300–1770 m/s from 0 K to 6000 K at core pressures, and the drop seems more remarkable for C and O than for the other two elements. For example, the maximal drop of $Fe_{60}C_4$ reaches 1770 m/s from 0 K to 6000 K. For binary alloys $Fe_{56}X_8$ (X = C, O, Si, and S), the effects of temperature and pressure are similar to those found for $Fe_{60}X_4$ (X = C, O, Si, and S). Our results indicate that increasing the content of light elements clearly influences the compressional sound velocity. The compressional sound velocities of $Fe_{60}X_4$ and $Fe_{56}X_8$ (X = C and O) at 4000–6000 K are close to the PREM data. In comparison with the content of light elements, temperature is the primary influence factor on the compressional sound velocity. Figure 5 presents the temperature variation of compressional sound velocity at 360 GPa and compares our results with those of previous *ab initio* molecular dynamics simulations. For pure hcp-iron, the variation of compressional sound velocity with temperature agrees well with the results in previous

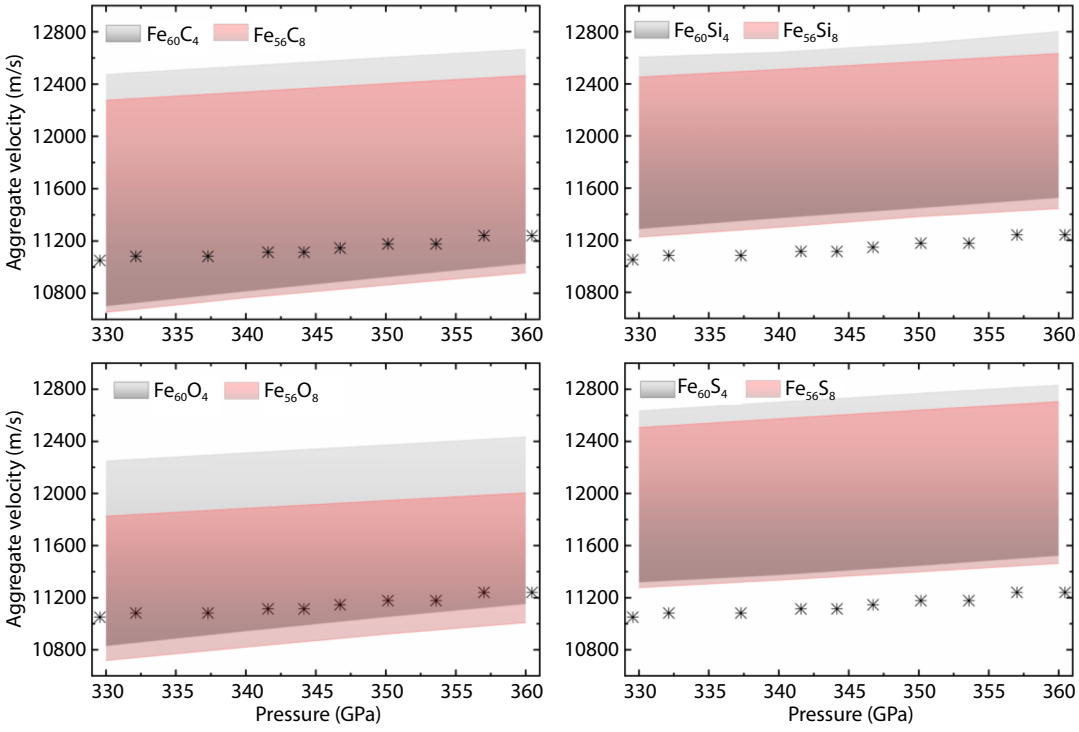

Figure 4. Calculated compressional sound velocity of $Fe_{60}X_4$ and $Fe_{56}X_8$ (X = C, O, Si, and S) at core pressures. The shaded areas enclose sound velocity range for temperature spanning between 0 and 6000 K from high to low. The solid stars indicate the PREM data.

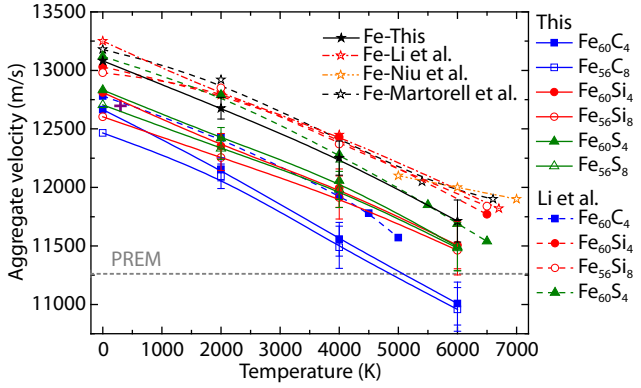

Figure 5. Calculated compressional sound velocity as a function of temperature for hcp-iron and its alloys at 360 GPa. The dashed lines stand for the PREM data. The cross represents the result of pure iron by second-order polynomial fitting from the experimental data of Mao HK et al. (1998, 2001) and theoretical data of Vočadlo et al. (2003).

simulations (Martorell et al., 2013a, b; Niu ZW et al., 2015; Li YG et al., 2018), though our values are slightly lower. It should be noted that the v_P values of pure iron in previous simulations (Martorell et al., 2013a, b; Niu ZW et al., 2015; Li YG et al., 2018) are larger than the v_P value derived by second-order polynomial fitting from the experimental data of Mao HK et al. (1998, 2001) and theoretical data of Vočadlo et al. (2003) at normal temperature. Our obtained values of v_P are slightly smaller than the former but obviously larger than the latter. Fortunately, the relative errors among these results are within 3%. The differences can be explained in various ways. For the results of Niu ZW et al. (2015), one possible reason is the underestimation of the C_{33}/C_{11} ratio, which was obtained on the base of long-wave limit approximation. In general, an accurate phonon spectrum is needed for long-wave limit approximation, especially for modes near the *G* point. This approximation will bring negative effects on the computation of elastic constants when the phonon frequencies exhibit certain softening. Second, the difference between our calculation and the calculation of Li YG et al. (2018) may be caused by different averaging; their calculations use the Voigt average, which calculates polycrystalline elastic moduli based on invariant strain and often overestimates the moduli; the alternative Reuss average, based on invariant stress, often underestimates them (see Table S6). For these reasons, we have chosen to use the VRH average.

In our calculations, the v_P results based on the VRH average are about 20–200 m/s lower than the v_P results based on the Voigt average, and high temperature leads to large difference (see Table S7). Another possible reason for differences between our results and those of Li GY et al. is that our calculations fitting the curves of elastic constants and pressures at different temperatures assume linear relationships. Apart from the reasons above, different potentials can differ in several GPa of elastic moduli, causing changes of sound velocity to a certain extent (Sun T et al, 2018; Li YG et al., 2018). Furthermore, the trend of density changes with temperature may also influence the calculations of compressional sound velocity. Overall, even at 6500 K, all of these AIMD simulation results for pure iron are much larger than the PREM data, which means that pure iron cannot alone account for the seismic observations. However, Figure 5 shows that, despite the introduction of light elements, the compressional sound velocity does not drop remarkably, except for alloys involving the element carbon. Our results show that the largest drop is not more than 600 m/s for the various binary alloys, which is similar to the results of Li YG et al. (2018) with the exception of $Fe_{60}C_4$ and $Fe_{56}C_8$; they report that the compressional sound velocity of binary alloy $Fe_{60}C_4$ decreases quickly with increasing temperature, as does that of binary alloy $Fe_{60}S_4$ when the temperature is higher than 5500 K. Our results also show that the compressional sound velocity of $Fe_{60}C_4$ and $Fe_{56}C_8$ are lower than the PREM data when the temperature is higher than 5000 K. These findings mean that high temperature has greater influence on the binary iron alloys than on pure iron. In general, combining the results of density and sound velocity in our calculations, we speculate that the highest contents of oxygen and carbon will not exceed 1.4 wt.% and 1.8 wt.% in the Earth's inner core. This means that the inner core is an oxygen-depleted environment, which is similar to the findings regarding the Earth's core by Huang HJ et al. (2011). In addition, if only hcp-Fe-Si binary alloys are considered, the Si content would be nearly 4 wt.% in the inner core, which is consistent with the estimated 4–8 wt.% of the ideal mixture model (Lin JF et al., 2003; Asanuma et al., 2011; Fischer et al., 2014). If only hcp-Fe-S binary alloys are taken into account, the S content becomes approximately 6 wt.%, close to the previous evaluation results from meteorites research (Alfè et al., 2000).

Because the ratio of compressional elastic moduli C_{33}/C_{11} is one common measure of elastic anisotropy for hcp-structured materials, we explored the relation of *c/a* and C_{33}/C_{11}; Figure 6 presents the results obtained from our calculations at 360 GPa. We find that high *c/a* is correlated with high elastic anisotropy where C_{33}/C_{11} is larger than 1. But no significant linear relation exists between the two quantities, and the relation is likely not unique. Hence, we caution against predicting the elastic anisotropy of C_{33}/C_{11} based on the ratio of *c/a*. Temperature correlation with C_{33}/C_{11} is more

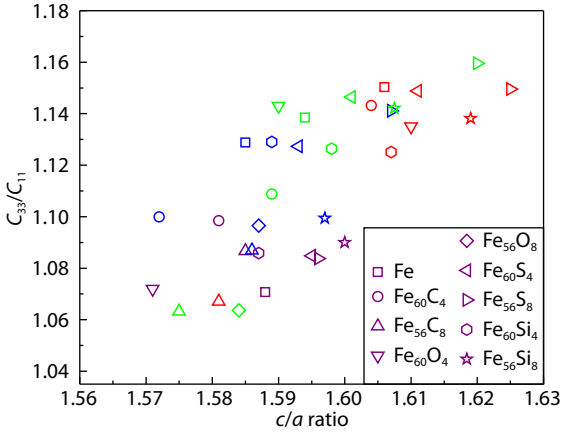

Figure 6. The relation between *c/a* axial ratio and the ratio of compressional elastic moduli C_{33}/C_{11} from our calculations at 360 GPa. The colors brown, blue, green, and red represent 0 K, 2000 K, 4000 K, and 6000 K, respectively.

significant than the ratio of c/a; the elastic anisotropy of C_{33}/C_{11} is above 1.0 at temperatures higher than 2000 K when c/a is fixed. This agrees with the calculations of Vočadlo et al. (2009). Furthermore, alloying iron with light element also considerably affects the C_{33}/C_{11} of hcp-Fe. The elastic anisotropies of C_{33}/C_{11} are larger than 1.1 at finite temperature when S or Si is included, but when C or O are included, most are smaller than 1.1. Hence, due to the influence of temperature and alloying, the relationship under core conditions between c/a and C_{33}/C_{11} is complicated and implicit.

3.2 Anisotropy of Iron Alloys and Implications for the Inner Core

Recently, many seismic studies have confirmed that the anisotropy of the inner core proves to be surprisingly more complex than previously thought (e.g. Niu FL and Wen LX, 2002; Lythgoe et al., 2014; Tkalčić, 2015). Pure iron alone does not have properties that could explain such complicated anisotropy, though most seismic models have tried to use the lattice preferred orientation (LPO) of iron crystals to explain the anisotropy of inner core (Sumita and Bergman, 2007). Hence, the following section focuses on the impact of light elements on the anisotropy of pure hcp-iron.

Figure 7 shows the variation of the computed relative P-wave velocity for hexagonal iron at 360 GPa, based on our, Li et al.'s, and Martorell's elastic properties at various temperatures; note that, at a certain temperature, our profile of the relative P-wave velocity variation curve is different from the profiles by Li YG et al. (2018), and Martorell et al. (2013b), which could be because of methodological differences. Nevertheless, we all report values relatively close to the IMIC model based on Wang et al.'s OIC model at high temperatures. Moreover, hexagonal iron shows greater P-wave anisotropy in these AIMD simulations compared with *ab initio* results at relatively low pressures (e.g. Vočadlo et al., 2009; Mattesini et al., 2010). Figure 8 presents calculated relative normalized P-wave velocities of the various binary alloys, based on their elastic properties at core pressures and at different temperatures. In general, temperature and the specific light-element content obviously affect the profiles of the relative P-wave velocity variation curves, while the effect of pressure becomes insignificant except in the case of O element alloys. For $Fe_{60}X_4$ (X = C, O, Si, and S), the profiles at high temperatures, compared with the profiles of variation curves of the relative P-wave velocity at 0 K, are closer to those of the IMIC model based on Wang et al.'s OIC model. At 0 K, in comparison with $Fe_{60}X_4$ (X = C, and Si), increasing the content of C and Si in $Fe_{56}X_8$ (X = C, and Si) makes the minima of the curves decline dramatically, while increasing the content of S in $Fe_{56}S_8$ has little impact on the curves. At high temperatures, increasing the content of light elements in $Fe_{56}X_8$ (X = C, O, Si, and S) sharply influences the curves, particularly in the cases of $Fe_{56}C_8$ at 6000 K and $Fe_{56}O_8$ at both 4000 K and 6000 K, where the trend of the curves even appears to reverse. This may be caused by the fact that the ratio of C_{33} and C_{11} is close to 1. Moreover, compared with the curves associated with three other light elements, those associated with S are affected primarily by temperature rather than by pressure and the level of content of light element. Figure 9 shows the variations of the calculated relative normalized P-wave velocity based on the elastic properties of binary iron alloy by Li YG et al. (2018) at 360 GPa and at different temperatures. It can be found that most of these relative velocity variations are close to those from the IMIC model based on Wang et al.'s model.

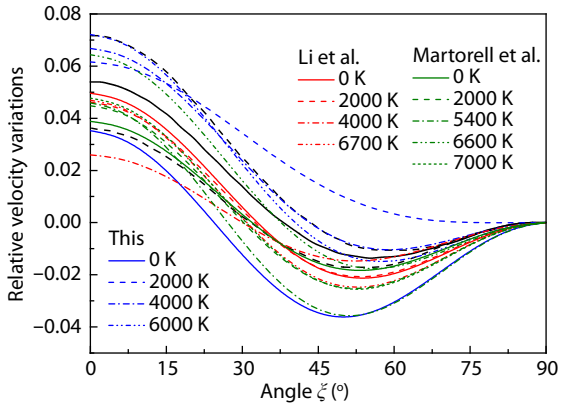

Figure 7. Variations of the computed relative P-wave velocity for hexagonal iron at 360 GPa based on elastic properties at various temperatures. Black solid lines represent best fitting IMIC model by Wang et al.'s model for OIC anisotropy corrections; black dash lines stand for the region of uncertainty in the IMIC model (Wang T et al., 2015; Romanowicz and Wenk, 2017).

The anisotropy strength of relative P-wave velocity at core pressures is presented in Figure 10; note that results with large deviation are not included. It can be seen that, for $Fe_{60}X_4$ (X = C, O, Si, and S), pressure has only a small effect on the anisotropy strength of relative P-wave velocity, but the effect of temperature is strong. With increasing temperature at a fixed pressure, the strength of anisotropy first decreases and then increases — except for $Fe_{60}O_4$, whose anisotropy strength increases continuously. This phenomenon could be an artifact of the calculation methods; results at zero temperature are calculated from the optimal structure while the results at finite temperature are calculated from average time-averaged structure. Furthermore, compared with other binary hcp-Fe alloys at 360 GPa and 6000 K, only the anisotropy strength of $Fe_{60}S_4$ exceeds 8.8%, the maximum inner core anisotropy at the western region (Lythgoe et al., 2014).

For $Fe_{56}X_8$ (X = C, O, Si, and S), the effect of pressure on the anisotropy strength is more complex than for $Fe_{60}X_4$ (X = C, O, Si, and S). For example, the anisotropy strength of $Fe_{56}C_8$ at 2000 K increases quickly with increasing pressure but at 4000 K it decreases quickly. The anisotropy strength of $Fe_{56}O_8$, however, exhibits the contrary pattern: it decreases quickly with rising pressure at 2000 K but at both 4000 K and 6000 K it increases quickly. As for $Fe_{56}Si_8$, pressure has negligible effect on its anisotropy at fixed temperatures except at 0 K. For $Fe_{56}S_8$, however, the anisotropy strength rises modestly as pressure increases at high temperatures, specifically at 2000 K, 4000 K, and 6000 K. Furthermore, similar to what we found for $Fe_{60}X_4$ (X = C, O, Si, and S), only the anisotropy strength of $Fe_{56}S_8$ exceeds 8.8% at 360 GPa and high temperatures, 4000 K and 6000 K, which may suggest that these alloys may explain the anisotropy of inner core.

However, combining the calculated densities and aggregate

velocities, Lythgoe et al. (2014) suggest that the binary hcp-Fe-S alloys have limitations in providing a good explanation for the anisotropy of inner core, particularly at the western region. Nevertheless, the anisotropy strength of these binary hcp-Fe alloys at high temperatures is close to or more than 8%, which is the maximum anisotropy estimated by Wang T et al. (2015). Considering the concentration of light elements, adding S and Si will cause the anisotropy strength to increase, especially in the range 350 to

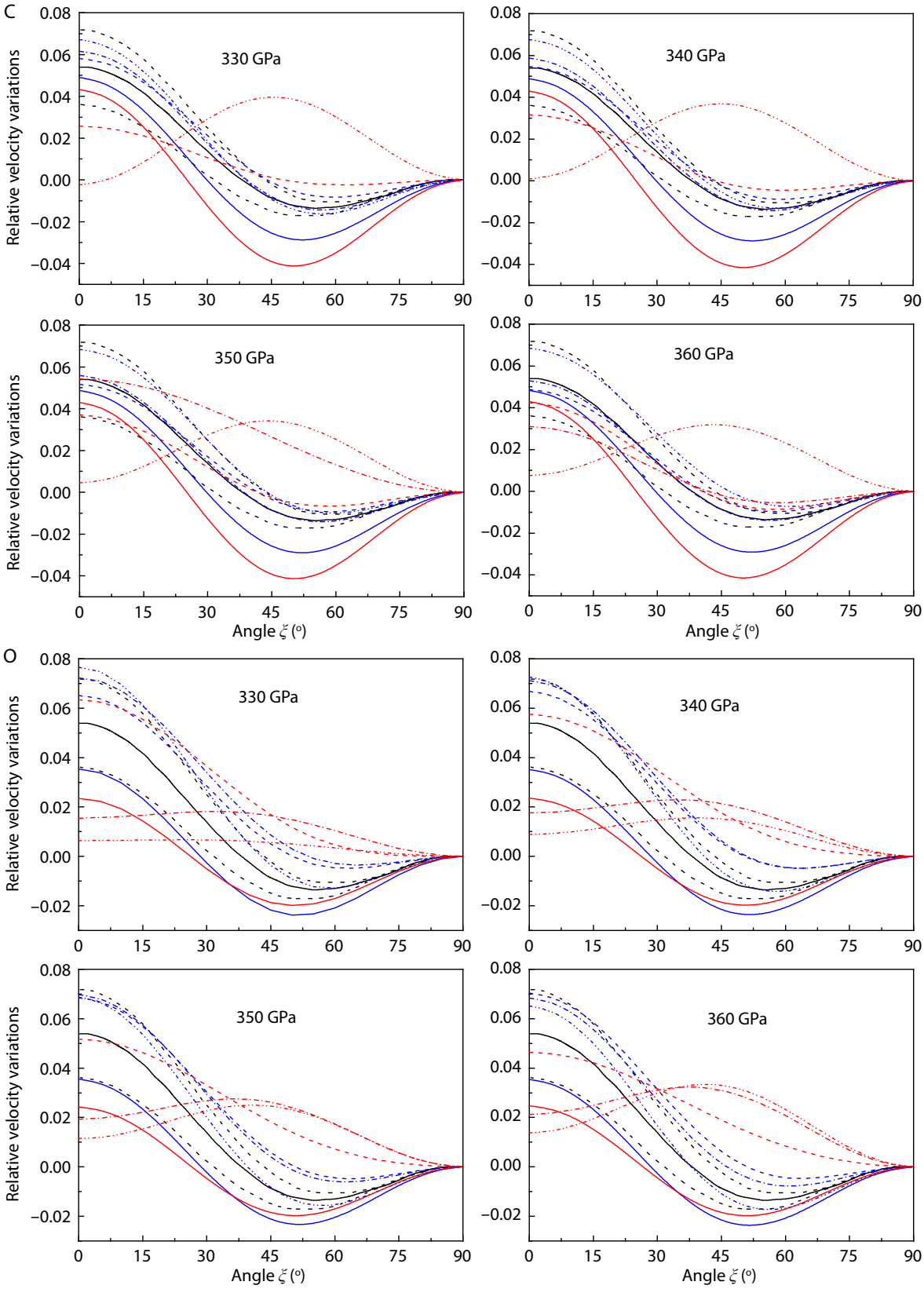

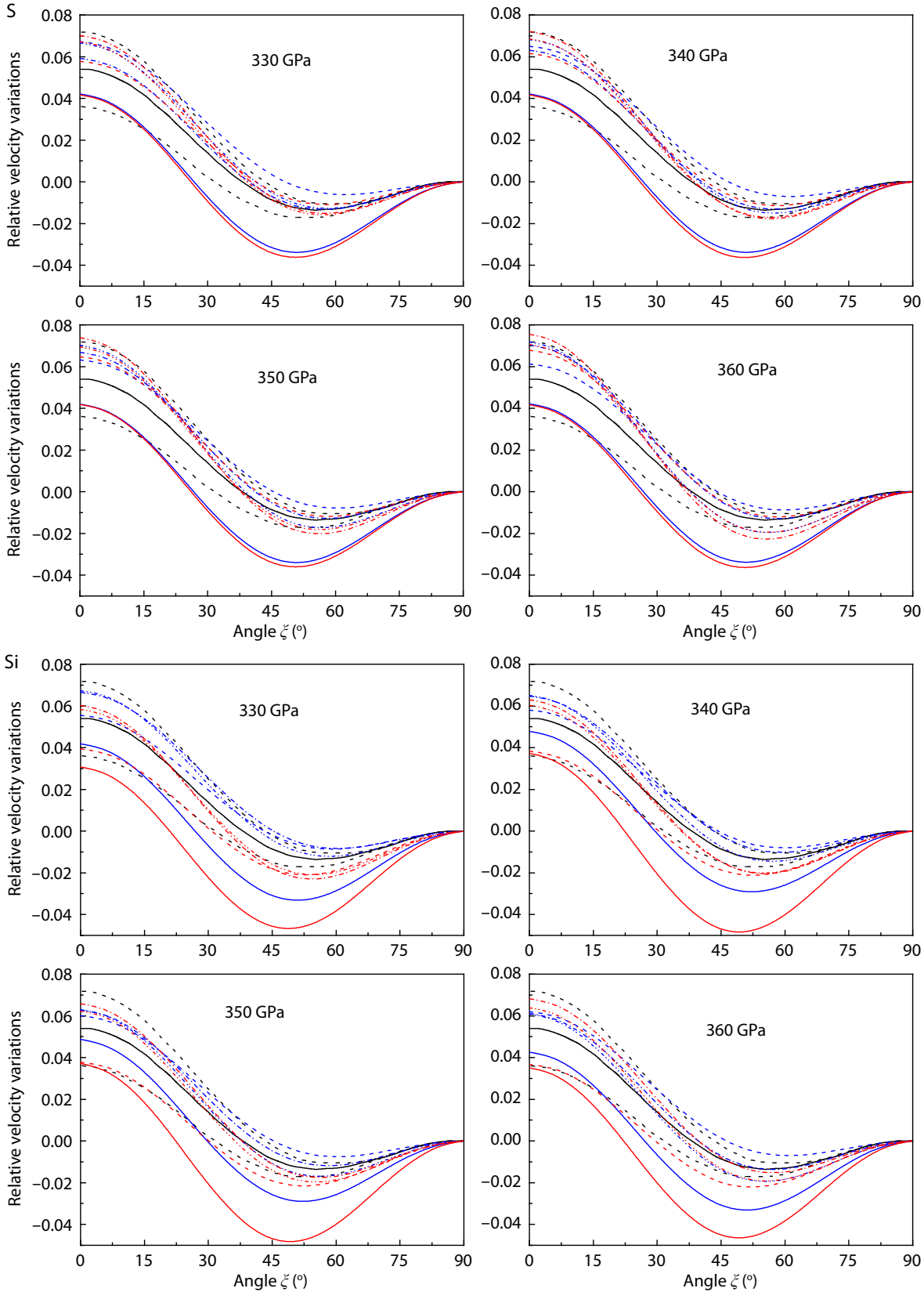

Figure 8. Calculated relative P-wave velocity variations of $Fe_{60}X_4$ and $Fe_{56}X_8$ (X = C, O, Si, and S) based on elastic properties at core pressures and different temperatures. Blue and red lines: respective relative P-wave velocity of $Fe_{60}X_4$ and $Fe_{56}X_8$. The solid, dash, dash dot, and dash dot dot lines indicate relative P-wave velocity at 0 K, 2000 K, 4000 K, and 6000 K, respectively. Black solid lines represent best fitting IMIC model by Wang et al.'s model for OIC anisotropy corrections; black dash lines stand for the region of uncertainty in the IMIC model (Wang T et al., 2015; Romanowicz and Wenk, 2017).

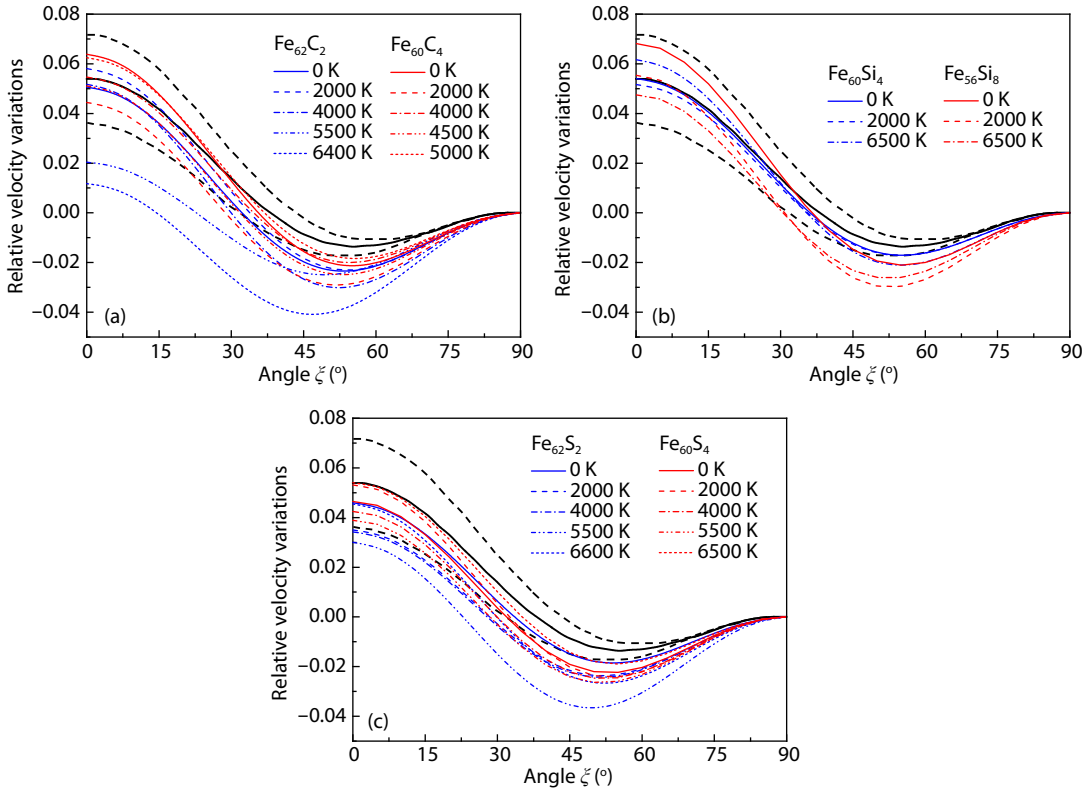

Figure 9. Calculated relative P-wave velocity variations of binary iron alloy based on the elastic properties obtained by Li YG et al. (2018) at 360 GPa and different temperatures. Black solid lines represent best fitting IMIC model by Wang et al.'s model for OIC anisotropy corrections; black dash lines stand for the region of uncertainty in the IMIC model (Wang T et al., 2015; Romanowicz and Wenk, 2017).

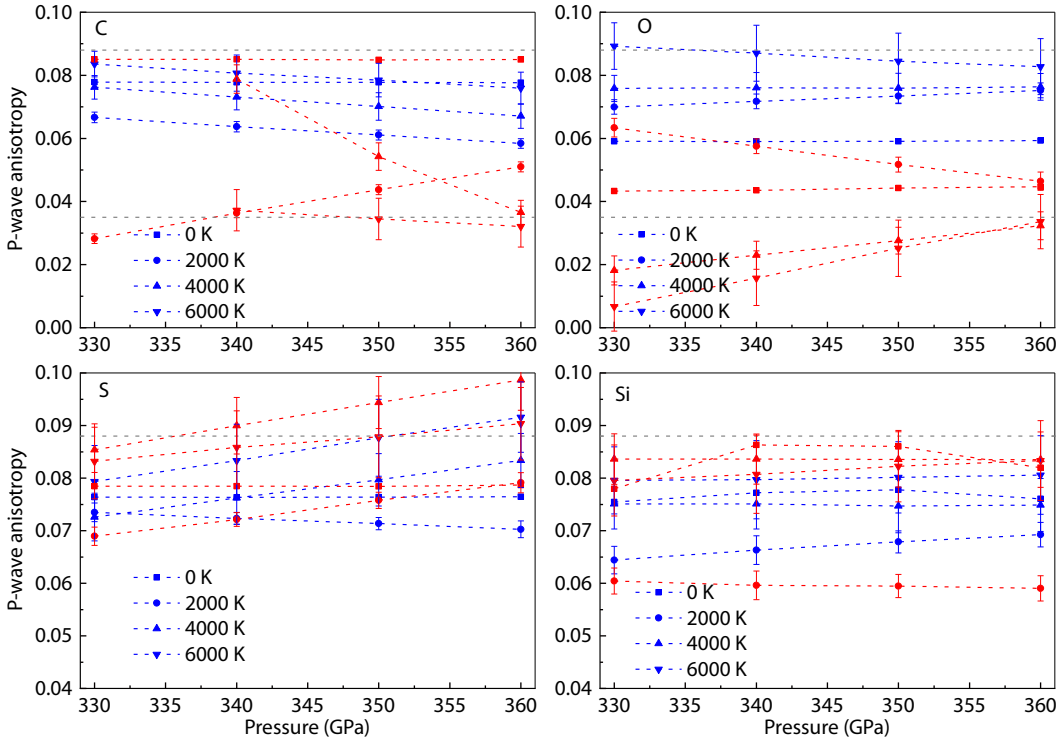

Figure 10. The anisotropy strength of P-wave relative velocity of $Fe_{60}X_4$ and $Fe_{56}X_8$ (X = C, O, Si, and S) at core pressures. The blue and red symbols represent the strength of anisotropy of $Fe_{60}X_4$ and $Fe_{56}X_8$, respectively. The grey dash lines indicate the minimum and maximum anisotropy of the inner core at its western region (Lythgoe et al., 2014).

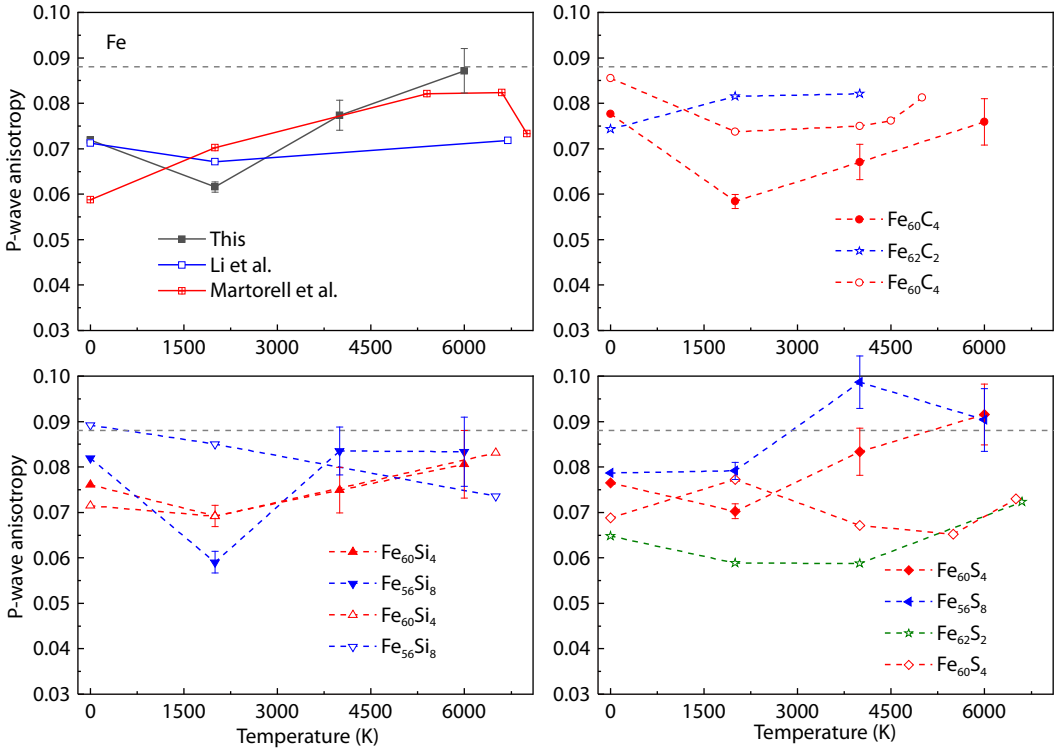

Figure 11. The strength of anisotropy of hcp-iron and its alloys based on relative P-wave velocity variations at 360 GPa and various temperatures, in comparison with available results. The open symbols represent the results of Li YG et al. (2018).The grey dash lines indicate the maximum anisotropy of the inner core at its western region (Lythgoe et al., 2014).

360 GPa. Conversely, adding C and O will decrease the anisotropy strength at all applied pressures and temperatures, expect zero temperature. This means that high content of C and O elements may not be appropriate to explain the strong anisotropy of inner core.

The computed strengths of the anisotropy of hcp-iron and its alloys at 360 GPa are illustrated in Figure 11, in comparison with different AIMD simulations. Consistency among the different calculations, but also significant differences, can be seen. Intriguingly, in most cases, both our results and those reported by Li YG et al. (2018) show similar increases of anisotropy strength with rising temperature. Compared with pure hcp-Fe, at some temperatures the introduction of light elements reduces, rather than increase the strength of the anisotropy. Considering that the temperature in the boundary of the inner core is probably far more than 4000 K, we find, based on these AIMD calculations, that increasing temperature, rather than increasing pressure, is likely to be the major factor causing the anisotropy to become stronger towards the center of inner core. In addition, taking into consideration the uncertainties in these calculations, we note that the strength of the anisotropy shows roughly an increasing trend with increasing concentrations of the light elements (Si and S) at a given temperature. On the contrary, with increasing concentrations of element C, the strength of the anisotropy shows a descending trend.

Multiple studies have indicated that the anisotropy of hcp-iron is associated with the *c*/*a* axial ratio, which means the elastic anisotropy can be constrained by a certain *c*/*a* ratio. In order to ensure full consideration of the impact of the *c*/*a* axial ratio, in our calculations we have explored the relationship between elastic anisotropy strength and *c*/*a* axial ratio. The results for iron and its various alloys are plotted in Figure 12. Due to the considerable deviation of the values, only a weak linearity can be detected between elastic anisotropy strength and *c*/*a* axial ratio. Furthermore, our results indicate that the influence of light elements is remarkable, which means that the elastic anisotropy strength may be changed by alloying. An effective light element such as S,

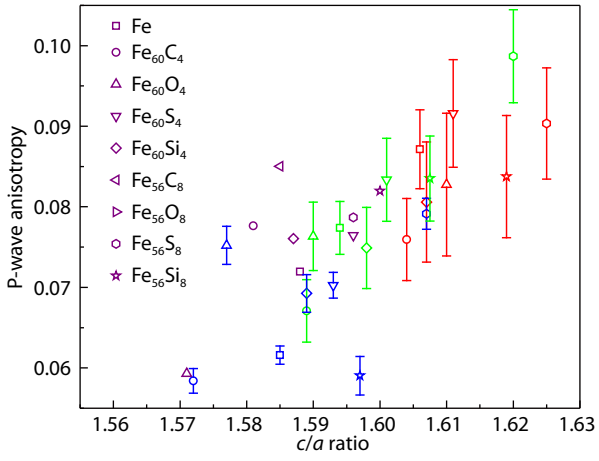

Figure 12. The correlation between axial ratio (*c*/*a*) and the strength of anisotropy of hcp-iron and its alloys at 360 GPa and various temperatures. The colors brown, blue, green, and red represent 0 K, 2000 K, 4000 K, and 6000 K, respectively.

rather than C or O, can raise the elastic anisotropy strength considerably, compared to that of hcp-Fe at the same temperature. For instance, the elastic anisotropy strength of $Fe_{60}S_4$ is 0.004 larger than that of hcp-Fe, while the anisotropy strength of $Fe_{60}O_4$ is 0.004 smaller than that of hcp-Fe at 6000 K. We therefore conclude that the anisotropy depends on combined effects of temperature and the type of alloying element.

For Earth's inner core, because of the improbable existence of a huge single crystal, the anisotropies of iron alloys must be 8% at least or even more than 8.8% to be able to account for the anisotropy of the inner core (Martorell et al., 2013a, b; Lythgoe et al., 2014; Wang T et al., 2015; Romanowicz and Wenk, 2017; Li YG et al., 2018). From these reliable AIMD calculations, only the Fe-S alloys appear able to account for an anisotropy strength of 8.8% or greater. The strength of anisotropy of the Fe-S alloys is larger than 9% at high temperature, while their aggregate velocities are far larger than the PREM data. These observations strongly suggest that the roles played by various light element binary alloys of iron in the behavior of the Earth's inner core are far from simple though they are likely to be important; caution is advised in attributing to them, singly or collectively, an explanation of the complex anisotropy of the inner core.

4. Conclusions

We have investigated the anisotropy of hcp-iron and eight kinds of hcp-Fe-X (X = C, O, Si, and S) binary alloy under inner core conditions based on *ab initio* molecular dynamics calculations. In these alloys, the anisotropy depends on combined effects of temperature and the type of light element. The impact of pressure on the anisotropy strength may reasonably be ignored, because it is far smaller than the impacts of temperature and the type of light element. More importantly, at inner core pressures the strengths of anisotropy of hcp-iron and these eight kinds of alloy vary non-linearly with increasing temperature. At high temperatures, alloying iron with some light elements, such as C or O, actually does not increase but decreases the strength of the anisotropy relative to that of pure iron. However, substituting the light element S can significantly increase the elastic anisotropy strength of hcp-Fe. Considering the limitations of the alloys data analyzed here, more detailed calculations, in which phase transitions and inelastic phenomena are also taken into account, are needed to clarify the effect of light elements on core anisotropy.

Acknowledgments

The authors are grateful to the editors and reviewers for their valuable comments, which helped to improve the original manuscript. This work is supported by the National Natural Science Foundation of China (Grant Nos. 41704088 and 11804284), and the Open Foundation of Hypervelocity Impact Research Center of CARDC (Grant No. 20200202). The thermoelastic data used are listed in the Supporting Information (SI).

References

Alfè, D., Gillan, M. J., and Price, G. D. (2000). Constraints on the composition of the Earth's core from *ab initio* calculations. *Nature*, *405*(6783), 172–175. https://doi.org/10.1038/35012056

Asanuma, H., Ohtani, E., Sakai, T., Terasaki, H., Kamada, S., Hirao, N., and Ohishi, Y. (2011). Static compression of $Fe_{0.83}Ni_{0.09}Si_{0.08}$ alloy to 374 GPa and $Fe_{0.93}Si_{0.07}$ alloy to 252 GPa: Implications for the Earth's inner core. *Earth Planet. Sci. Lett.*, *310*(1-2), 113–118. https://doi.org/10.1016/j.epsl.2011.06.034

Bazhanova, Z. G., Roizen, V. V., and Oganov, A. R. (2017). High-pressure behavior of the Fe-S system and composition of the earth's inner core. *Phys.-Usp.*, *60*(10), 1025–1032. https://doi.org/10.3367/UFNe.2017.03.038079

Beghein, C., and Trampert, J. (2003). Robust normal mode constraints on inner-core anisotropy from model space search. *Science*, *299*(5606), 552–555. https://doi.org/10.1126/science.1078159

Belonoshko, A. B., Ahuja, R., and Johansson, B. (2003). Stability of the body-centred-cubic phase of iron in the earth's inner core. *Nature*, *424*(6952), 1032–1034. https://doi.org/10.1038/nature01954

Belonoshko, A. B., Li, S., Ahuja, R., and Johansson, B. (2004). High-pressure crystal structure studies of Fe, Ru and Os. *J. Phys. Chem. Solids*, *65*(8-9), 1565–1571. https://doi.org/10.1016/j.jpcs.2003.11.043

Belonoshko, A. B., Skorodumova, N. V., Davis, S., Osiptsov, A. N., Rosengren, A., and Johansson, B. (2007). Origin of the low rigidity of the earth's inner core. *Science*, *316*(5831), 1603–1605. https://doi.org/10.1126/science.1141374

Belonoshko, A. B., Lukinov, T., Fu, J., Zhao, J. J., Davis, S., and Simak, S. I. (2017). Stabilization of body-centred cubic iron under inner-core conditions. *Nat. Geosci.*, *10*(4), 312–316. https://doi.org/10.1038/ngeo2892

Blöchl, P. E. (1994). Projector augmented-wave method. *Phys. Rev. B*, *50*(24), 17953–17979. https://doi.org/10.1103/PhysRevB.50.17953

Buffett, B. A., and Wenk, H. R. (2001). Texturing of the Earth's inner core by Maxwell stresses. *Nature*, *413*(6851), 60–63. https://doi.org/10.1038/35092543

Creager, K. C. (1992). Anisotropy of the inner core from differential travel times of the phases PKP and PKIKP. *Nature*, *356*(6367), 309–314. https://doi.org/10.1038/356309a0

Dziewonski, A. M., and Anderson, D. L. (1981). Preliminary reference Earth model. *Phys. Earth Planet. Inter.*, *25*(4), 297–356. https://doi.org/10.1016/0031-9201(81)90046-7

Fischer, R. A., Campbell, A. J., Reaman, D. M., Miller, N. A., Heinz, D. L., Dera, P., and Prakapenka, V. B. (2013). Phase relations in the Fe–FeSi system at high pressures and temperatures. *Earth Planet. Sci. Lett.*, *373*, 54–64. https://doi.org/10.1016/j.epsl.2013.04.035

Fischer, R. A., Campbell, A. J., Caracas, R., Reaman, D. M., Heinz, D. L., Dera, P., and Prakapenka, V. B. (2014). Equations of state in the Fe-FeSi system at high pressures and temperatures. *J. Geophys. Res.*, *119*(4), 2810–2827. https://doi.org/10.1002/2013jb010898

Flyvbjerg, H., and Petersen, H. G. (1989). Error estimates on averages of correlated data. *J. Chem. Phys.*, *91*(1), 461–466. https://doi.org/10.1063/1.457480

Ganz, E., Ganz, A. B., Yang, L. M., and Dornfeld, M. (2017). The initial stages of melting of graphene Between 4000 K and 6000 K. *Phys. Chem. Chem. Phys.*, *19*(5), 3756–3762. https://doi.org/10.1039/C6CP06940A

Hill, R. (1952). The elastic behaviour of a crystalline aggregate. *Proc. Phys. Soc., Sect. A*, *65*(5), 349-354. https://doi.org/10.1088/0370-1298/65/5/307

Hirose, K., Morard, G., Sinmyo, R., Umemoto, K., Hernlund, J., Helffrich, G., and Labrosse, S. (2017). Crystallization of silicon dioxide and compositional evolution of the Earth's core. *Nature*, *543*(7643), 99–102. https://doi.org/10.1038/nature21367

Huang, H. J., Fei, Y. W., Cai, L. C., Jing, F. Q., Hu, X. J., Xie, H. S., Zhang, L. M., and Gong, Z. Z (2011). Evidence for an oxygen-depleted liquid outer core of the Earth. *Nature*, *479*(7374), 513-516. https://doi.org/10.1038/nature10621

Jeanloz, R., and Wenk, H. R. (1988). Convection and anisotropy of the inner core. *Geophys. Res. Lett.*, *15*(1), 72–75. https://doi.org/10.1029/GL015i001p00072

Kresse, G., and Furthmüller, J. (1996). Efficient iterative schemes for *ab initio* total-energy calculations using a plane-wave basis set. *Phys. Rev. B*, *54*(16), 11169–11186. https://doi.org/10.1103/physrevb.54.11169

Kresse, G., and Joubert, D. (1999). From ultrasoft pseudopotentials to the projector augmented-wave method. *Phys. Rev. B*, *59*(3), 1758–1775. https://doi.org/10.1103/PhysRevB.59.1758

Page, L. Y., and Saxe, P. (2002). Symmetry-general least-squares extraction of

elastic data for strained materials from *ab initio* calculations of stress. *Phys. Rev. B*, *65*(10), 104104. https://doi.org/10.1103/PhysRevB.65.104104

Li, Y. G., Vočadlo, L., Brodholt, J., and Wood, I. G. (2016). Thermoelasticity of Fe_7C_3 under inner core conditions. *J. Geophys. Res.*, *121*(8), 5828–5837. https://doi.org/10.1002/2016JB013155

Li, Y. G., Vočadlo, L., and Brodholt, J. P. (2018). The elastic properties of *hcp*-Fe alloys under the conditions of the Earth's inner core. *Earth Planet. Sci. Lett.*, *493*, 118–127. https://doi.org/10.1016/j.epsl.2018.04.013

Lin, J. F., Campbell, A. J., Heinz, D. L., and Shen, G. Y. (2003). Static compression of iron-silicon alloys: Implications for silicon in the Earth's core. *J. Geophys. Res.*, *108*(B1), 2045. https://doi.org/10.1029/2002JB001978

Lincot, A., Merkel, S., and Cardin, P. (2015). Is inner core seismic anisotropy a marker for plastic flow of cubic iron?. *Geophys. Res. Lett.*, *42*(5), 1326–1333. https://doi.org/10.1002/2014GL062862

Lythgoe, K. H., Deuss, A., Rudge, J. F., and Neufeld, J. A. (2014). Earth's inner core: Innermost inner core or hemispherical variations?. *Earth Planet. Sci. Lett.*, *385*, 181–189. https://doi.org/10.1016/j.epsl.2013.10.049

Mao, H. K., Shu, J. F., Shen, G. Y., Hemley, R. J., Li, B. S., and Singh, A. K. (1998). Elasticity and rheology of iron above 220 GPa and the nature of the Earth's inner core. *Nature*, *396*(6713), 741–743. https://doi.org/10.1038/25506

Mao, H. K., Xu, J., Struzhkin, V. V., Shu, J., Hemley, R. J., Sturhahn, W., Hu, M. Y., Alp, E. E., Vocadlo, L., Wortmann, G. (2001). Phonon density of states of iron up to 153 gigapascals. *Science*, *292*(5518), 914–916. https://doi.org/10.1126/science.1057670

Martorell, B., Brodholt, J., Wood, I. G., and Vočadlo, L. (2013a). The effect of nickel on the properties of iron at the conditions of Earth's inner core: *ab initio* calculations of seismic wave velocities of Fe–Ni alloys. *Earth Planet. Sci. Lett.*, *365*, 143–151. https://doi.org/10.1016/j.epsl.2013.01.007

Martorell, B., Vočadlo, L., Brodholt, J., and Wood, I. G. (2013b). Strong premelting effect in the elastic properties of hcp-Fe under inner-core conditions. *Science*, *342*(6157), 466–468. https://doi.org/10.1126/science.1243651

Martorell, B., Wood, I. G., Brodholt, J., and Vočadlo, L. (2016). The elastic properties of hcp-$Fe_{1-x}Si_x$ at Earth's inner-core conditions. *Earth Planet. Sci. Lett.*, *451*, 89–96. https://doi.org/10.1016/j.epsl.2016.07.018

Mattesini, M., Belonoshko, A. B., Buforn, E., Ramírez, M., Simak, S. I., Udías, A., Mao, H. K., and Ahuja, R. (2010). Hemispherical anisotropic patterns of the Earth's inner core. *Proc. Nat. Acad. Sci. USA*, *107*(21), 9507–9512. https://doi.org/10.1073/pnas.1004856107

Merkel, S., Liermann, H. P., Miyagi, L., and Wenk, H. R. (2013). In situ radial X-ray diffraction study of texture and stress during phase transformations in bcc-, fcc- and hcp-iron up to 36 GPa and 1000 K. *Acta Mater.*, *61*(14), 5144–5151. https://doi.org/10.1016/j.actamat.2013.04.068

Mermin, N. D. (1965). Thermal properties of the inhomogeneous electron gas. *Phys. Rev.*, *137*(5A), A1441–A1443. https://doi.org/10.1103/PhysRev.137.A1441

Moakher, M., and Norris, A. N. (2006). The closest elastic tensor of arbitrary symmetry to an elasticity tensor of lower symmetry. *J. Elast.*, *85*(3), 215–263. https://doi.org/10.1007/s10659-006-9082-0

Morelli, A., Dziewonski, A. M., and Woodhouse, J. H. (1986). Anisotropy of the inner core inferred from *PKIKP* travel times. *Geophys. Res. Lett.*, *13*(13), 1545–1548. https://doi.org/10.1029/GL013i013p01545

Morrison, R. A., Jackson, J. M., Sturhahn, W., Zhang, D. Z., and Greenberg, E. (2018). Equations of State and Anisotropy of Fe-Ni-Si Alloys. *J. Geophys. Res.*, *123*(6), 4647–4675. https://doi.org/10.1029/2017JB015343

Niu, F. L., and Wen, L. X. (2002). Seismic anisotropy in the top 400 km of the inner core beneath the "eastern" hemisphere. *Geophys. Res. Lett.*, *29*(12), 1611. https://doi.org/10.1029/2001GL014118

Niu, Z. W., Zeng, Z. Y., Cai, L. C., and Chen, X. R. (2015). Study of the thermodynamic stability of iron at inner core from first-principles theory combined with lattice dynamics. *Phys. Earth Planet. Inter.*, *248*, 12–19. https://doi.org/10.1016/j.pepi.2015.09.002

Nosé, S. (1984). A molecular dynamics method for simulations in the canonical ensemble. *Mol. Phys.*, *52*(2), 255–268. https://doi.org/10.1080/00268978400101201

Panda, K. B., and Chandran, K. S. R. (2006). Determination of elastic constants of titanium diboride (TiB_2) from first principles using FLAPW implementation of the density functional theory. *Comp. Mater. Sci.*, *35*(2), 134–150. https://doi.org/10.1016/j.commatsci.2005.03.012

Perdew, J. P., Burke, K., and Ernzerhof, M. (1996). Generalized gradient approximation made simple. *Phys. Rev. Lett.*, *77*(18), 3865–3868. https://doi.org/10.1103/PhysRevLett.77.3865

Reuss, A., and Angew, Z. (1929). Berechnung del fliessgrenze von misch-kristallen auf grund der plastizitatbedingung for einkristalle. *Math. Mech.*, *9*(1), 49–58.

Romanowicz, B., Cao, A. M., Godwal, B., Wenk, R., Ventosa, S., and Jeanloz, R. (2016). Seismic anisotropy in the Earth's innermost inner core: testing structural models against mineral physics predictions. *Geophys. Res. Lett.*, *43*(1), 93–100. https://doi.org/10.1002/2015gl066734

Romanowicz, B., and Wenk, H. R. (2017). Anisotropy in the deep Earth. *Phys. Earth Planet. Inter.*, *269*, 58–90. https://doi.org/10.1016/j.pepi.2017.05.005

Sakai, T., Takahashi, S., Nishitani, N., Mashino, I., Ohtani, E., and Hirao, N. (2014). Equation of state of pure iron and $Fe_{0.9}Ni_{0.1}$ alloy up to 3 Mbar. *Phys. Earth Planet. Inter.*, *228*, 114–126. https://doi.org/10.1016/j.pepi.2013.12.010

Sha, X. W., and Cohen, R. E. (2006). Thermal effects on lattice strain in ε-Fe under pressure. *Phys. Rev. B*, *74*, 064103. https://doi.org/10.1103/PhysRevB.74.064103

Sha, X. W., and Cohen, R. E. (2010a). First-principles thermal equation of state and thermoelasticity of hcp Fe at high pressures. *Phys. Rev. B*, *81*(9), 094105. https://doi.org/10.1103/PhysRevB.81.094105

Sha, X. W., and Cohen, R. E. (2010b). Elastic isotropy of ε-Fe under earth's core conditions. *Geophys. Res. Lett.*, *37*(10), L10302. https://doi.org/10.1029/2009GL042224

Steinle-Neumann, G., Stixrude, L., and Cohen, R. E. (1999). First-principles elastic constants for the hcp transition metals Fe, Co, and Re at high pressure. *Phys. Rev. B*, *60*(2), 791–799. https://doi.org/10.1103/physrevb.60.791

Sumita, I., and Bergman, M. I. (2007). Inner-core dynamics. *Treat. Geophys.*, *8*, 299–318. https://doi.org/10.1016/B978-044452748-6.00132-2

Sun, T., Brodholt, J. P., Li, Y. G., and Vočadlo, L. (2018). Melting properties from *ab initio* free energy calculations: Iron at the Earth's inner-core boundary. *Phys. Rev. B*, *98*(22), 224301. https://doi.org/10.1103/PhysRevB.98.224301

Tateno, S., Hirose, K., Ohishi, Y., and Tatsumi, Y. (2010). The structure of iron in earth's inner core. *Science*, *330*(6002), 359–361. https://doi.org/10.1126/science.1194662

Tateno, S., Hirose, K., Komabayashi, T., Ozawa, H., and Ohishi, Y. (2012). The structure of Fe-Ni alloy in Earth's inner core. *Geophys. Res. Lett.*, *39*(12), L12305. https://doi.org/10.1029/2012GL052103

Tkalčić, H. (2015). Complex inner core of the Earth: the last frontier of global seismology. *Rev. Geophys.*, *53*(1), 59–94. https://doi.org/10.1002/2014RG000469

Vočadlo, L., Alfè, D., Gillan, M. J., and Price, G. D. (2003). The properties of iron under core conditions from first principles calculations. *Phys. Earth Planet. Inter.*, *140*(1-3), 101–125. https://doi.org/10.1016/j.pepi.2003.08.001

Vočadlo, L. (2007). Ab initio calculations of the elasticity of iron and iron alloys at inner core conditions: evidence for a partially molten inner core?. *Earth Planet. Sci. Lett.*, *254*(1-2), 227–232. https://doi.org/10.1016/j.epsl.2006.09.046

Vočadlo, L., Dobson, D. P., and Wood, I. G. (2009). *Ab initio* calculations of the elasticity of hcp-Fe as a function of temperature at inner-core pressure. *Earth Planet. Sci. Lett.*, *288*(3-4), 534–538. https://doi.org/10.1016/j.epsl.2009.10.015

Voigt, W. (1928). *Lehrbuch der Kristallphysik*: *Teubner-Leipzig*. New York: Macmillan.

Wang, T., Song, X. D., and Xia, H. H. (2015). Equatorial anisotropy in the inner part of earth's inner core from autocorrelation of earthquake coda. *Nat. Geosci.*, *8*(3), 224–227. https://doi.org/10.1038/ngeo2354

Wenk, H. R., Baumgardner, J. R., Lebensohn, R. A., and Tomé, C. N. (2000). A convection model to explain anisotropy of the inner core. *J. Geophys. Res.*, *105*(B3), 5663–5677. https://doi.org/10.1029/1999jb900346

Woodhouse, J. H., Giardini, D., and Li, X. D. (1986). Evidence for inner core anisotropy from free oscillations. *Geophys. Res. Lett.*, *13*(13), 1549–1552. https://doi.org/10.1029/gl013i013p01549

Supplementary Materials for "The anisotropy of hexagonal close-packed iron under inner core conditions: the effect of light elements"

Introduction

We report the details of the process of calculating the elastic constants and the elastic anisotropy for hcp-Fe and its alloys. To confirm the simulated structures are solids, the root-mean-square displacement and radial distribution function analyses for *ab initio* molecular dynamics (AIMD) simulations are presented in Figure S1. The calculated elastic constants for $Fe_{60}X_4$ (X = C, O, Si, and S) are shown in Figure S2. Taking $Fe_{60}S_4$ as an example, the equilibrium axial ratio *c/a* corresponding to the lowest statistical average energy $\bar{E}_{\rm min}$ are shown in Figure S3 by numerical fitting the data of statistical average energy $\bar{E}$ and axial ratio *c/a* at the given volume 420.7 Å^3. Taking $Fe_{60}X_4$ (X = C, O, Si, and S) as an example, the computed unit cell parameters and the forces at different directions are given in Table S1 and Table S2, respectively. The calculated isothermal elastic constants with errors are listed in Table S3 and S4. To demonstrate the validity of elastic constants, the analysis of variance for the linear fitting of C_{44} is shown in Table S5. In order to exclude the influence of different average methods, taking $Fe_{60}Si_4$ as an example, the strength of anisotropy of acoustic velocity obtained with Voigt, Reuss, and VRH average methods is compared, as listed in Table S6. The comparison of acoustic velocity for pure iron, $Fe_{60}X_4$, and $Fe_{56}X_8$ (X = C, O, Si, and S) obtained with Voigt and VRH average methods at 360 GPa are listed in Table S7.

Text S1: The State of the Simulated Structures

To confirm the simulated structures are solids, both the root-mean-square displacements (RMSD) and the radial distribution function (RDF) were retrieved for the last 3 ps of each AIMD simulation. Our AIMD tests with the simulation time of 8, 10, and 12 ps show that the system is in equilibrium for the last 3 ps in three cases, and the state of the simulated structures can be analyzed from the simulation of the last 3 ps. On the other hand, similar operation can be found in the literature (Martorell et al., 2013). As an example, the RMSDs and RDFs of $Fe_{60}X_4$ (X = C, O, Si, and S) are exhibited in Figure S1. Their RMSDs generally oscillate around a constant value with time, which is the typical behavior of solids. The corresponding RDFs indicate that there exist two well-defined peaks for the first and second coordination shells. Both RMSDs and RDFs demonstrate that the simulated structures are solids.

Text S2: Analysis of Variance for Linear Fitting of Elastic Constants and Pressures

To demonstrate the validity of elastic constants, we calculate the Degree-of-freedom adjusted coefficient of determination (Adj. R-Square) and take analysis of variance for the linear fitting. It is found that the Adj. R-Squares of the elastic constants except C_{44} are greater than 0.97, which means the linear fitting is reliable. For C_{44}, the Adj. R-Square lies in the range from 0.83 to 0.93 (Table S5). In order to validate the reliability of the linear fitting of C_{44}, an analysis of variance is needed. The *P*-value and *F*-value are measures of statistical evidence in analysis of variance. The results suggest that the *F*-values are larger than 29 and the *P*-values are much less than 0.01, which verifies the reliability of the linear fitting of C_{44} and the trustworthy precision. Furthermore, C_{44} is relatively small compared to the other elastic constants and has an insignificant contribution to the aggregated properties. The influence of fitting error of C_{44} on the calculation of aggregated sound velocity is no more than 1%.

Text S3: The Anisotropy with Different Average Methods

The strength of anisotropy is obtained based on the calculated elastic constants, and therefore the strength of anisotropy error mainly comes from the propagation of the errors of the elastic constants. In order to exclude the influence of different average methods, the strength of anisotropy of acoustic velocity obtained with different average methods are tested. As an example, the test results of $Fe_{60}Si_4$ are listed in Table S6. It shows that the gap of the strength of anisotropy is only 0.0009 between Voigt–Reuss–Hill (VRH) average and other average methods. The strength of anisotropy of acoustic velocity is a relative value, and the differences of different average methods are not more than 0.002 in all of our simulations.

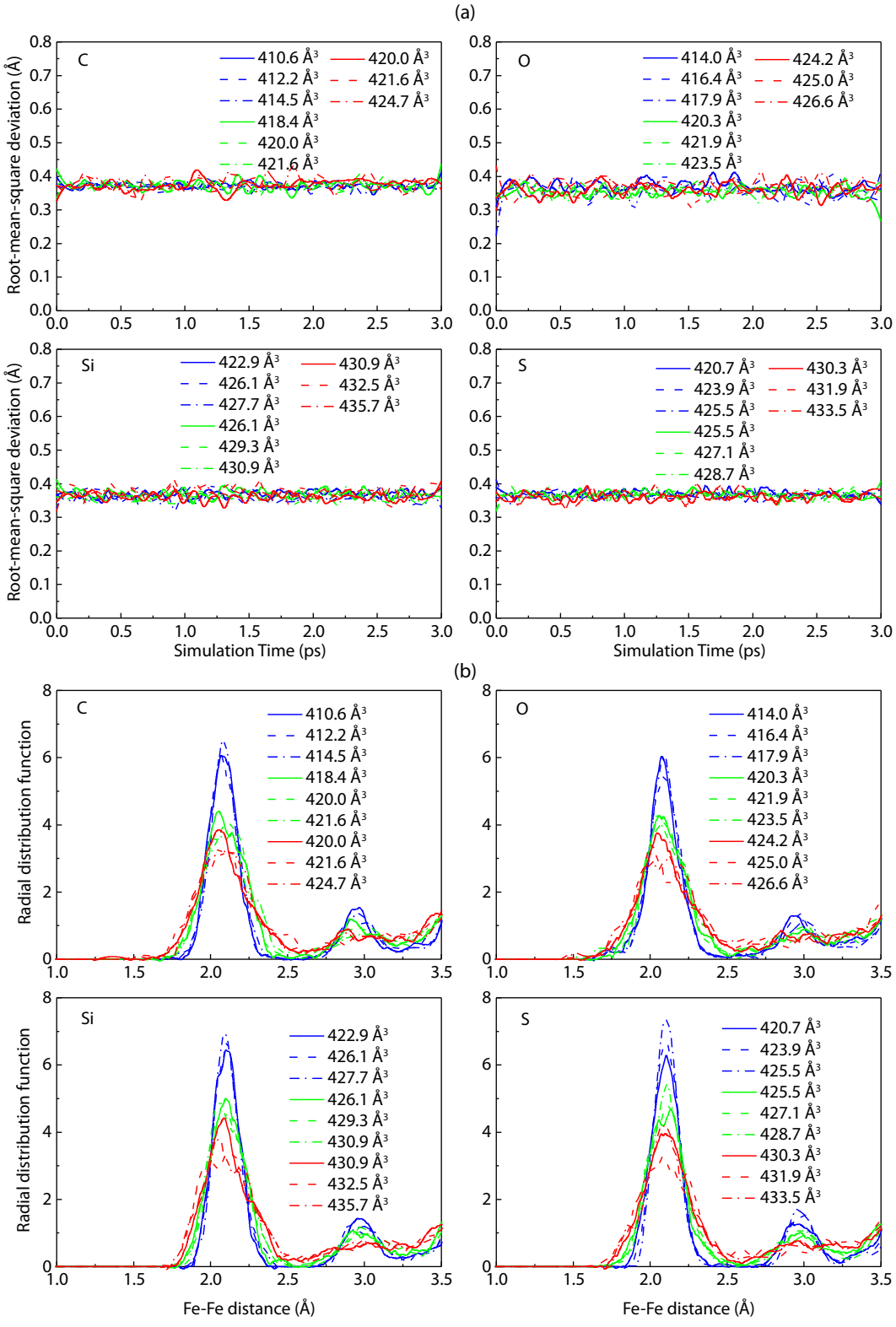

Figure S1. Root-mean-square displacement (a) and radial distribution function (b) analysis for $Fe_{60}X_4$ (X = C, O, Si, and S) as a function of the temperature for the last 3 ps of AIMD simulation. The colors with blue, green, and red represent 2000 K, 4000 K, and 6000 K, respectively.

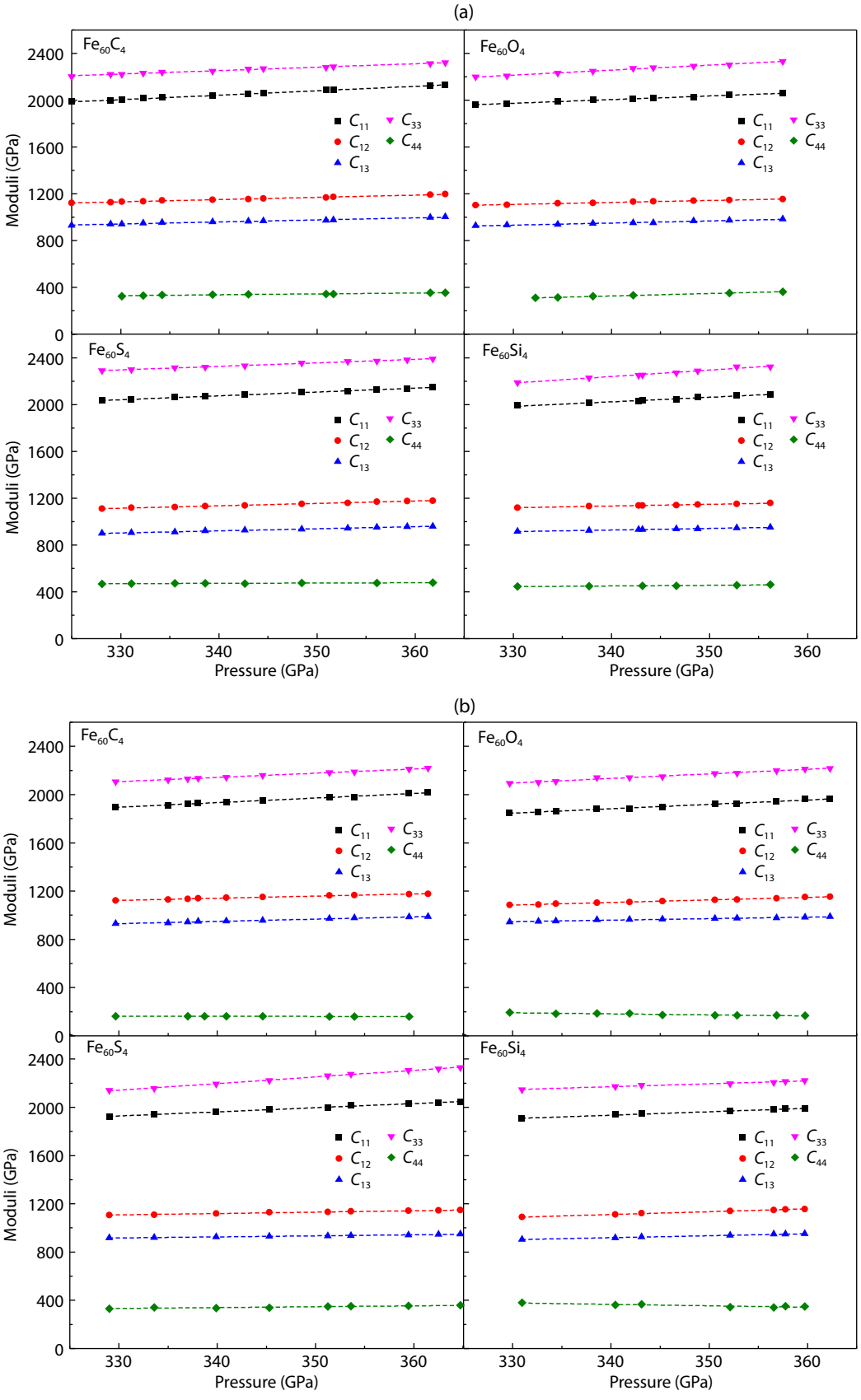
(a)
$Fe_{60}C_4$
$Fe_{60}O_4$
$Fe_{60}S_4$
$Fe_{60}Si_4$
C_{11}
C_{12}
C_{13}
C_{33}
C_{44}
Moduli (GPa)
Pressure (GPa)
(b)
$Fe_{60}C_4$
$Fe_{60}O_4$
$Fe_{60}S_4$
$Fe_{60}Si_4$
C_{11}
C_{12}
C_{13}
C_{33}
C_{44}
Moduli (GPa)
Pressure (GPa)

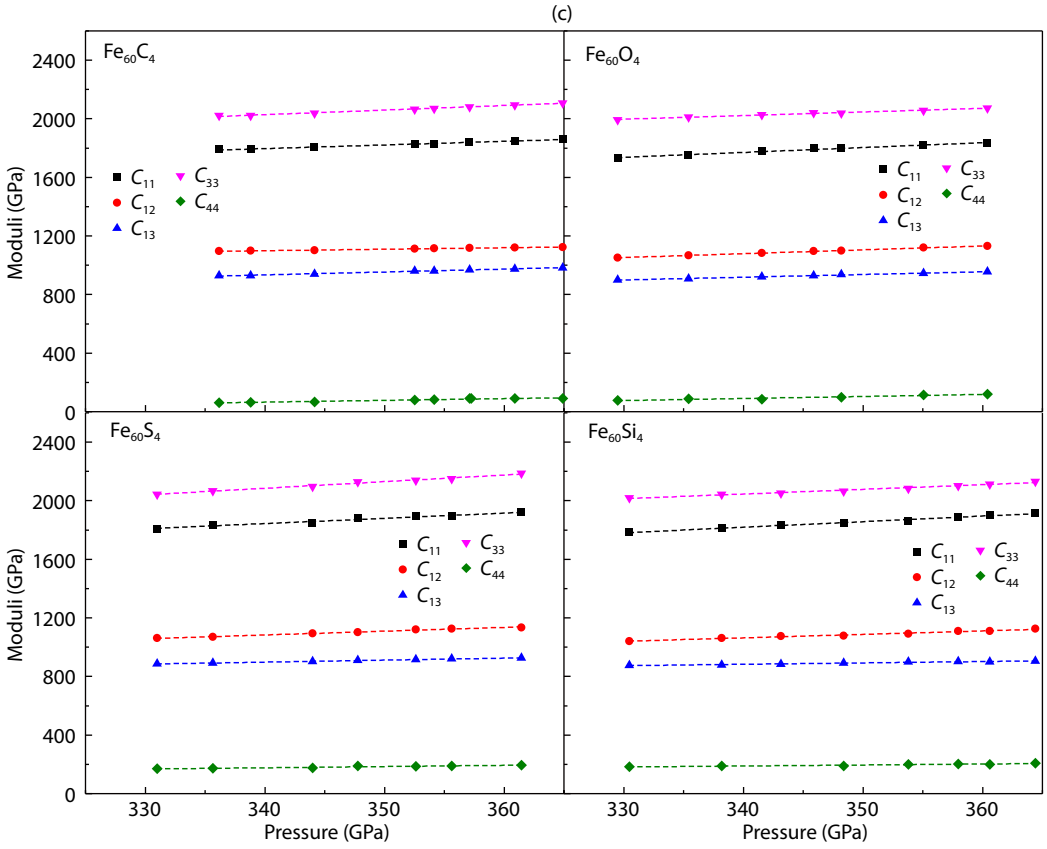

Figure S2. The calculated elastic constants of $Fe_{60}X_4$ (X = C, O, Si, and S) as a function of the pressure at 2000 K (a), 4000 K (b), and 6000 K (c), respectively.

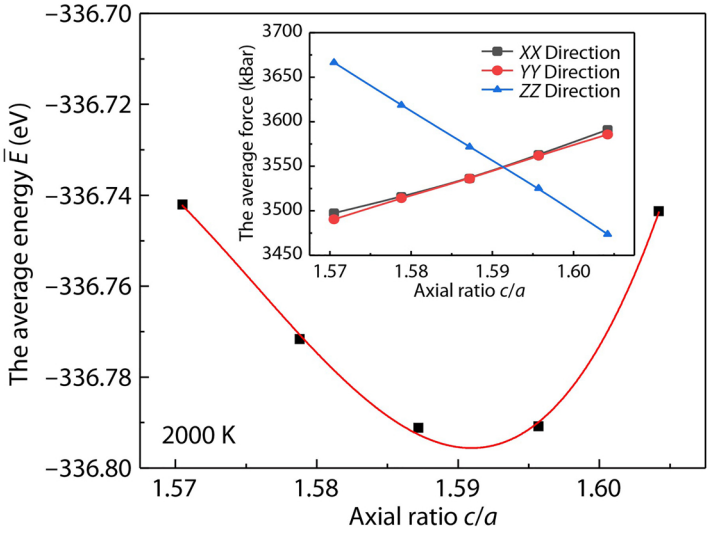

Figure S3. The relationship of statistical average energy $\bar{E}$ and axial ratio *c/a* at the given volume 420.7 Å^3. The inset shows the results of corresponding average force.

Table S1. The computed supercell parameters of $Fe_{60}X_4$ (X = C, O, Si, and S) with 64 atoms. The ratio of c/a is twice of c_{super}/a_{super} ratio.

	T (K)	V (Å^3)	P (GPa)	a_{super} (Å)	c_{super} (Å)	c/a
	2000	410.6	358.8	8.450	6.641	1.572
	2000	412.2	353.1	8.458	6.653	1.573
	2000	414.5	344.5	8.476	6.662	1.572
	4000	418.4	350.1	8.476	6.725	1.587
$Fe_{60}C_4$	4000	420.0	345.6	8.484	6.737	1.588
	4000	421.6	339.6	8.499	6.739	1.586
	6000	420.0	368.5	8.453	6.787	1.606
	6000	421.6	361	8.467	6.790	1.604
	6000	424.7	349.8	8.490	6.804	1.603
	2000	414.0	356.5	8.466	6.671	1.576
	2000	416.4	347.9	8.482	6.684	1.576
	2000	417.9	342.3	8.492	6.692	1.576
	4000	420.3	352.2	8.485	6.741	1.589
$Fe_{60}O_4$	4000	421.9	347	8.497	6.747	1.588
	4000	423.5	341.5	8.506	6.758	1.589
	6000	424.2	359.3	8.474	6.822	1.61
	6000	425.0	355.9	8.479	6.826	1.61
	6000	426.6	351.3	8.495	6.826	1.607
	2000	420.7	355	8.482	6.752	1.592
	2000	423.9	343.6	8.504	6.769	1.592
	2000	425.5	338	8.514	6.778	1.592
	4000	425.5	356	8.502	6.797	1.599
$Fe_{60}S_4$	4000	427.1	350.5	8.513	6.806	1.599
	4000	428.7	345.2	8.521	6.817	1.6
	6000	430.3	358.2	8.514	6.854	1.61
	6000	431.9	353.5	8.523	6.865	1.611
	6000	433.5	347.8	8.536	6.871	1.61
	2000	422.9	353.5	8.504	6.752	1.588
	2000	426.1	342.3	8.525	6.769	1.588
	2000	427.7	337.1	8.538	6.775	1.587
	4000	426.1	359.1	8.508	6.797	1.598
$Fe_{60}Si_4$	4000	429.3	348.3	8.530	6.812	1.597
	4000	430.9	342.6	8.543	6.817	1.596
	6000	430.9	360.3	8.523	6.849	1.607
	6000	432.5	355	8.537	6.851	1.605
	6000	435.7	344.4	8.561	6.865	1.604

Note. T is temperature, V is volume of supercell and P is pressure.

Table S2. The force (GPa) of $Fe_{60}X_4$ (X = C, O, Si, and S) on cell in Cartesian coordinates at different directions.

	V (Å^3)	*XX* (GPa)	*YY* (GPa)	*ZZ* (GPa)	*XY* (GPa)	*YZ* (GPa)	*ZX* (GPa)
	410.6	358.7	358.8	358.8	0.01	0.09	−0.08
$Fe_{60}C_4$-2000 K	412.2	353.2	353.1	353.0	0.10	0.11	0.08
	414.5	344.5	344.7	344.4	0.05	−0.04	−0.08
	418.4	350.1	350.0	349.9	−0.02	0.29	−0.17
$Fe_{60}C_4$-4000 K	420.0	345.8	345.4	345.5	0.21	−0.25	−0.18
	421.6	339.4	339.9	339.6	−0.27	−0.13	−0.16
	420.0	368.2	368.5	368.8	0.62	0.50	0.81
$Fe_{60}C_4$-6000 K	421.6	361.0	361.4	360.5	0.72	−0.59	−0.02
	424.7	349.2	350.3	349.8	0.41	−0.47	0.52
	414.0	356.6	356.4	356.6	0.12	−0.08	−0.13
$Fe_{60}O_4$-2000 K	416.4	347.9	348.0	347.7	0.15	0.16	−0.09
	417.9	342.2	342.6	342.1	0.12	0.12	−0.10
	420.3	352.4	351.9	352.2	0.17	0.18	0.17
$Fe_{60}O_4$-4000 K	421.9	346.8	346.9	347.1	0.32	0.18	−0.16
	423.5	341.5	341.8	340.9	−0.33	0.16	−0.21
	424.2	359.6	358.5	357.7	−0.48	0.69	−0.17
$Fe_{60}O_4$-6000 K	425.0	355.2	352.9	353.8	0.16	−0.56	−0.67
	426.6	351.8	351.5	352.2	−0.65	−0.33	0.65
	420.7	355.0	355.2	354.8	−0.01	0.14	0.11
$Fe_{60}S_4$-2000 K	423.9	343.7	343.8	343.4	0.16	−0.03	−0.07
	425.5	338.3	338.1	337.9	−0.18	0.06	0.10
	425.5	356.0	356.4	356.0	−0.21	−0.31	0.10
$Fe_{60}S_4$-4000 K	427.1	350.3	350.3	350.6	0.10	0.19	−0.28
	428.7	345.0	345.1	345.1	0.08	0.36	−0.32
	430.3	358.4	357.9	358.2	0.05	0.32	0.02
$Fe_{60}S_4$-6000 K	431.9	353.4	353.2	353.8	0.49	0.13	0.04
	433.5	347.5	347.8	347.8	0.24	−0.06	−0.01
	422.9	353.5	353.3	353.9	−0.14	−0.07	−0.12
$Fe_{60}Si_4$-2000 K	426.1	342.3	341.9	342.6	−0.02	0.13	−0.18
	427.7	337.1	337.1	336.8	0.14	−0.14	−0.06
	426.1	359.2	359.3	358.9	−0.00	−0.31	0.19
$Fe_{60}Si_4$-4000 K	429.3	348.4	348.0	348.0	0.38	−0.15	0.20
	430.9	342.7	342.8	342.5	−0.01	0.16	0.24
	430.9	360.8	360.1	360.1	−0.36	−0.21	0.62
$Fe_{60}Si_4$-6000 K	432.5	355.1	355.3	354.8	−0.46	0.71	0.67
	435.7	344.6	344.3	344.4	−0.17	−0.63	−0.47

Table S3. Calculated isothermal elastic constants of $Fe_{60}X_4$ (X = C, O, Si, and S) at different pressure (P) and temperature (T). The values in brackets are the errors of the elastic constants.

	P (GPa)	T (K)	C_{11} (GPa)	C_{12} (GPa)	C_{13} (GPa)	C_{33} (GPa)	C_{44} (GPa)
	330	2000	2004 (16)	1131 (11)	942 (8)	2224 (16)	329 (5)
$Fe_{60}C_4$	330	4000	1896 (23)	1123 (16)	930 (14)	2107 (22)	164 (6)
	330	6000	1742 (26)	1069 (21)	894 (17)	1967 (30)	53 (9)
	330	2000	1974 (16)	1109 (11)	932 (9)	2214 (20)	302 (6)
$Fe_{60}O_4$	330	4000	1847 (22)	1085 (15)	947 (13)	2096 (26)	191 (9)
	330	6000	1737 (27)	1053 (19)	900 (16)	1997 (31)	76 (16)
	330	2000	2042 (12)	1115 (11)	903 (9)	2297 (15)	470 (7)
$Fe_{60}S_4$	330	4000	1928 (24)	1108 (14)	917 (13)	2142 (27)	332 (19)
	330	6000	1808 (31)	1057 (22)	884 (16)	2040 (35)	168 (18)
	330	2000	1985 (17)	1119 (11)	915 (8)	2185 (19)	445 (9)
$Fe_{60}Si_4$	330	4000	1906 (23)	1088 (16)	903 (13)	2147 (27)	378 (20)
	330	6000	1781 (29)	1040 (20)	874 (17)	2014 (34)	182 (17)
	340	2000	2042 (17)	1150 (11)	959 (9)	2253 (16)	336 (5)
$Fe_{60}C_4$	340	4000	1934 (24)	1141 (16)	949 (14)	2142 (22)	162 (6)
	340	6000	1777 (27)	1079 (21)	914 (18)	2008 (30)	65 (9)
	340	2000	2005 (16)	1126 (11)	950 (9)	2257 (20)	324 (6)
$Fe_{60}O_4$	340	4000	1883 (23)	1106 (15)	959 (14)	2134 (27)	182 (10)
	340	6000	1770 (28)	1079 (19)	918 (16)	2022 (32)	90 (16)
	340	2000	2075 (12)	1135 (11)	921 (9)	2327 (16)	473 (7)
$Fe_{60}S_4$	340	4000	1962 (24)	1119 (14)	926 (14)	2197 (27)	340 (20)
	340	6000	1844 (32)	1083 (22)	898 (17)	2085 (36)	177 (18)
	340	2000	2024 (17)	1134 (11)	929 (9)	2240 (20)	450 (9)
$Fe_{60}Si_4$	340	4000	1935 (23)	1111 (16)	919 (13)	2171 (27)	366 (20)
	340	6000	1819 (30)	1064 (21)	883 (17)	2046 (34)	189 (18)
	350	2000	2080 (17)	1169 (11)	977 (9)	2282 (17)	344 (5)
$Fe_{60}C_4$	350	4000	1971 (25)	1159 (17)	968 (14)	2177 (22)	161 (6)
	350	6000	1801 (27)	1099 (21)	934 (18)	2040 (31)	77 (10)
	350	2000	2036 (16)	1143 (11)	968 (9)	2300 (20)	346 (6)
$Fe_{60}O_4$	350	4000	1919 (23)	1127 (15)	972 (14)	2172 (27)	174 (10)
	350	6000	1804 (28)	1105 (19)	937 (17)	2047 (32)	104 (16)
	350	2000	2108 (12)	1156 (11)	939 (9)	2357 (16)	475 (7)
$Fe_{60}S_4$	350	4000	1997 (24)	1131 (14)	934 (14)	2252 (27)	347 (20)
	350	6000	1880 (33)	1109 (22)	911 (17)	2130 (37)	185 (19)
	350	2000	2063 (17)	1148 (11)	942 (9)	2295 (21)	456 (9)
$Fe_{60}Si_4$	350	4000	1973 (24)	1135 (17)	936 (14)	2195 (28)	354 (21)
	350	6000	1857 (30)	1087 (21)	893 (17)	2078 (35)	195 (18)
	360	2000	2118 (17)	1189 (11)	994 (9)	2312 (17)	351 (5)
$Fe_{60}C_4$	360	4000	2009 (25)	1177 (17)	986 (15)	2213 (23)	160 (6)
	360	6000	1826 (27)	1099 (21)	954 (18)	2071 (31)	89 (10)
	360	2000	2067 (17)	1159 (11)	986 (9)	2343 (21)	368 (6)
$Fe_{60}O_4$	360	4000	1955 (24)	1148 (16)	984 (14)	2210 (28)	165 (10)
	360	6000	1837 (29)	1131 (19)	955 (17)	2071 (33)	118 (17)
	360	2000	2141 (13)	1176 (11)	957 (9)	2387 (16)	478 (7)
$Fe_{60}S_4$	360	4000	2031 (25)	1142 (15)	943 (14)	2307 (28)	354 (21)
	360	6000	1915 (33)	1135 (23)	925 (17)	2175 (38)	193 (19)
	360	2000	2102 (18)	1163 (12)	955 (9)	2351 (21)	461 (9)
$Fe_{60}Si_4$	360	4000	1991 (24)	1158 (17)	952 (14)	2219 (28)	343 (21)
	360	6000	1895 (31)	1111 (21)	902 (18)	2110 (35)	202 (18)

Table S4. Calculated isothermal elastic constants of $Fe_{56}X_8$ (X = C, O, Si, and S) at different pressures and temperatures. The values in brackets are the errors of the elastic constants.

	P (GPa)	*T* (K)	C_{11} (GPa)	C_{12} (GPa)	C_{13} (GPa)	C_{33} (GPa)	C_{44} (GPa)
	330	2000	1897 (14)	1180 (8)	1016 (11)	1986 (21)	296 (7)
$Fe_{56}C_8$	330	4000	1763 (27)	1129 (20)	1096 (19)	1918 (29)	176 (8)
	330	6000	1609 (30)	1083 (19)	1059 (17)	1602 (27)	47 (5)
	330	2000	1766 (15)	1108 (12)	1046 (12)	1974 (17)	263 (7)
$Fe_{56}O_8$	330	4000	1757 (28)	1075 (16)	1024 (17)	1807 (27)	168 (9)
	330	6000	1606 (30)	1112 (18)	980 (19)	1625 (32)	77 (8)
	330	2000	1924 (12)	1113 (9)	997 (9)	2129 (15)	406 (7)
$Fe_{56}S_8$	330	4000	1808 (21)	1063 (17)	919 (15)	2050 (27)	318 (13)
	330	6000	1747 (27)	1041 (19)	918 (16)	1971 (32)	190 (16)
	330	2000	1895 (15)	1131 (11)	1005 (11)	2029 (17)	360 (7)
$Fe_{56}Si_8$	330	4000	1794 (27)	1076 (17)	938 (15)	1994 (30)	315 (18)
	330	6000	1725 (31)	1047 (18)	887 (17)	1915 (34)	180 (19)
	340	2000	1934 (14)	1198 (8)	1026 (11)	2046 (22)	306 (7)
$Fe_{56}C_8$	340	4000	1685 (27)	1155 (20)	1085 (19)	1943 (29)	166 (8)
	340	6000	1639 (31)	1108 (20)	1065 (17)	1642 (27)	60 (5)
	340	2000	1813 (15)	1144 (13)	1052 (13)	2007 (17)	275 (7)
$Fe_{56}O_8$	340	4000	1763 (29)	1108 (16)	1054 (17)	1820 (27)	159 (9)
	340	6000	1624 (30)	1125 (19)	1015 (19)	1651 (32)	89 (8)
	340	2000	1960 (12)	1132 (9)	1009 (9)	2183 (16)	413 (7)
$Fe_{56}S_8$	340	4000	1852 (21)	1077 (17)	930 (15)	2107 (28)	323 (13)
	340	6000	1773 (27)	1067 (19)	928 (16)	2005 (32)	191 (17)
	340	2000	1932 (16)	1152 (11)	1015 (11)	2065 (17)	371 (7)
$Fe_{56}Si_8$	340	4000	1813 (27)	1111 (18)	955 (16)	2025 (31)	324 (19)
	340	6000	1742 (31)	1067 (19)	904 (17)	1941 (35)	186 (19)
	350	2000	1971 (14)	1217 (9)	1035 (11)	2105 (22)	316 (7)
$Fe_{56}C_8$	350	4000	1786 (28)	1182 (20)	1074 (20)	1969 (30)	157 (8)
	350	6000	1669 (31)	1134 (20)	1072 (17)	1683 (28)	71 (5)
	350	2000	1860 (16)	1181 (13)	1058 (13)	2039 (17)	287 (7)
$Fe_{56}O_8$	350	4000	1769 (29)	1142 (17)	1084 (18)	1832 (28)	150 (9)
	350	6000	1641 (30)	1137 (19)	1051 (19)	1676 (33)	102 (8)
	350	2000	1996 (13)	1150 (9)	1022 (9)	2236 (16)	420 (8)
$Fe_{56}S_8$	350	4000	1906 (21)	1100 (18)	951 (15)	2174 (28)	329 (13)
	350	6000	1800 (28)	1093 (20)	939 (17)	2039 (33)	191 (17)
	350	2000	1968 (16)	1173 (12)	1025 (11)	2102 (17)	381 (8)
$Fe_{56}Si_8$	350	4000	1832 (28)	1147 (18)	972 (16)	2057 (32)	332 (19)
	350	6000	1759 (32)	1087 (19)	920 (17)	1967 (35)	192 (20)
	360	2000	2008 (14)	1235 (9)	1045 (11)	2165 (23)	327 (7)
$Fe_{56}C_8$	360	4000	1887 (28)	1208 (21)	1063 (20)	1995 (31)	148 (8)
	360	6000	1699 (32)	1159 (20)	1079 (17)	1723 (28)	83 (6)
	360	2000	1907 (16)	1217 (13)	1065 (13)	2172 (17)	299 (7)
$Fe_{56}O_8$	360	4000	1775 (30)	1176 (17)	1114 (18)	1845 (28)	142 (9)
	360	6000	1659 (30)	1150 (19)	1086 (20)	1702 (33)	114 (9)
	360	2000	2032 (13)	1168 (9)	1034 (9)	2289 (16)	428 (8)
$Fe_{56}S_8$	360	4000	1940 (22)	1103 (18)	951 (15)	2221 (29)	334 (13)
	360	6000	1826 (28)	1119 (20)	949 (17)	2073 (33)	192 (18)
	360	2000	2005 (16)	1194 (12)	1035 (11)	2138 (17)	391 (8)
$Fe_{56}Si_8$	360	4000	1851 (29)	1182 (18)	989 (16)	2088 (32)	341 (19)
	360	6000	1777 (32)	1107 (19)	936 (18)	1993 (36)	198 (20)

Table S5. The analysis of variance for the linear fitting of C_{44} of $Fe_{60}X_4$ (X = C, O, Si, and S) at different temperatures.

	Adj. R-square	Mean square	*F*-value	*P*-value
$Fe_{60}C_4$-2000 K	0.929	692.032	106.183	1.755×10^{-5}
$Fe_{60}C_4$-4000 K	0.877	12.162	51.074	3.784×10^{-4}
$Fe_{60}C_4$-6000 K	0.927	1129.411	102.835	1.951×10^{-5}
$Fe_{60}O_4$-2000 K	0.958	4499.990	182.773	2.846×10^{-6}
$Fe_{60}O_4$-4000 K	0.842	617.770	43.753	3.002×10^{-4}
$Fe_{60}O_4$-6000 K	0.924	1383.866	62.125	1.4×10^{-3}
$Fe_{60}S_4$-2000 K	0.866	67.113	46.115	4.99×10^{-4}
$Fe_{60}S_4$-4000 K	0.855	560.069	42.293	6.295×10^{-4}
$Fe_{60}S_4$-6000 K	0.877	492.679	43.929	1.18×10^{-3}
$Fe_{60}Si_4$-2000 K	0.850	140.455	29.272	5.65×10^{-3}
$Fe_{60}Si_4$-4000 K	0.830	972.558	30.025	2.76×10^{-3}
$Fe_{60}Si_4$-6000 K	0.836	419.103	31.522	2.48×10^{-3}

Table S6. The comparison of the strength of anisotropy of acoustic velocity for $Fe_{60}Si_4$ obtained with different average methods, together with bulk modulus *B*, shear modulus *G*, and isotropic wave propagation velocity v_{p0}.

P (GPa)	*T* (K)	*B* (GPa)	*G* (GPa)	v_{p0} (km/s)	The anisotropy strength	Method
		1340	478	12.17	0.0641	Voigt
330	2000	1340	467	12.13	0.0624	Reuss
		1340	473	12.15	0.0633	VRH
		1305	437	11.97	0.0753	Voigt
330	4000	1304	423	11.91	0.0734	Reuss
		1305	430	11.94	0.0744	VRH
		1238	331	11.40	0.0798	Voigt
330	6000	1238	275	11.14	0.0781	Reuss
		1238	303	11.27	0.0789	VRH
		1364	488	12.24	0.0665	Voigt
340	2000	1364	477	12.20	0.0647	Reuss
		1364	483	12.22	0.0656	VRH
		1326	435	11.99	0.0753	Voigt
340	4000	1326	419	11.93	0.0735	Reuss
		1326	427	11.96	0.0744	VRH
		1260	340	11.48	0.08	Voigt
340	6000	1260	283	11.22	0.0782	Reuss
		1260	312	11.35	0.0791	VRH
		1387	499	12.31	0.0673	Voigt
350	2000	1387	487	12.26	0.0654	Reuss
		1387	493	12.29	0.0663	VRH
		1347	433	12.02	0.0748	Voigt
350	4000	1347	414	11.94	0.073	Reuss
		1347	423	11.98	0.0739	VRH

Continued from Table S6

P (GPa)	*T* (K)	*B* (GPa)	*G* (GPa)	v_{p0} (km/s)	The anisotropy strength	Method
350	6000	1282	349	11.56	0.0805	Voigt
		1282	291	11.30	0.0788	Reuss
		1282	320	11.43	0.0796	VRH
360	2000	1411	509	12.38	0.0683	Voigt
		1410	497	12.33	0.0671	Reuss
		1411	503	12.35	0.0675	VRH
360	4000	1369	431	12.04	0.0751	Voigt
		1369	410	11.95	0.0734	Reuss
		1369	421	11.99	0.0742	VRH
360	6000	1304	358	11.63	0.0809	Voigt
		1304	300	11.38	0.0793	Reuss
		1304	329	11.51	0.0801	VRH

Table S7. The comparison of acoustic velocity for pure iron, $Fe_{60}X_4$, and $Fe_{56}X_8$ (X = C, O, Si, and S) obtained with Voigt and VRH average methods at 360 GPa.

	T (K)	$Fe_{60}C_4$	$Fe_{56}C_8$	$Fe_{60}Si_4$	$Fe_{56}Si_8$	$Fe_{60}S_4$	$Fe_{56}S_8$	Fe	Method
v_p (m/s)	0	12689	12503	12836	12640	12857	12739	13104	Voigt
		12665	12465	12812	12603	12832	12705	13082	VRH
v_p (m/s)	2000	12203	12127	12377	12270	12445	12353	12695	Voigt
		12155	12095	12352	12254	12420	12334	12676	VRH
v_p (m/s)	4000	11746	11615	12036	11943	12106	12027	12281	Voigt
		11557	11489	11994	11914	12057	11982	12251	VRH
v_p (m/s)	6000	11283	11106	11614	11553	11633	11591	11780	Voigt
		11007	10957	11506	11463	11493	11483	11712	VRH